

Open-Source Benchtop Magnetophotometer (MAP) for Characterizing the Magnetic Susceptibility of Nanoparticles

Alexis Scholtz^{1,2}, Jack Paulson^{2,3}, Victoria Nuñez⁴, and Andrea M. Armani^{1,2,3,*}

¹Alfred E. Mann Department of Biomedical Engineering, University of Southern California, Los Angeles, CA 90089, USA

²Ellison Medical Institute, Los Angeles, CA 90064, USA

³Mork Family Department of Chemical Engineering and Materials Science, University of Southern California, Los Angeles, CA 90089, USA

⁴Thomas Lord Department of Computer Science, University of Southern California, Los Angeles, CA 90089, USA

*aarmani@emila.org

Abstract:

Magnetic nanoparticles form the foundation of many biomedical and environmental technologies. Although various methods exist to characterize a subset of physical properties of nanoparticles, measuring their magnetic response remains challenging. This property is defined by magnetic susceptibility, which describes how a material responds to an external magnetic field. However, accurately measuring magnetic susceptibility relies on specialized, high-performance instrumentation which require large quantities of dried sample. Here, we present the design and validation of an open-source benchtop instrument, a magnetophotometer (MAP), which non-destructively measures the magnetic susceptibility of suspended nanoparticles via monochromatic differential optical spectroscopy. To validate the system's accuracy, a series of measurements are performed, and results from a superconducting quantum interference device (SQUID) serve as a benchmark. First, a series of three iron oxide nanoparticle batches was synthesized with distinctly different susceptibility values, and the MAP successfully differentiates between them in agreement with SQUID results. Notably, in comparison with the SQUID, the MAP requires an order of magnitude less sample and obtains a result 99.8% faster. To demonstrate utility in the biomedical field, the MAP performs non-destructive analysis of bioconjugated magnetic nanoparticles, a measurement that is not possible using currently available commercial systems. The bioactivity of the surface coating is not degraded by the testing, and the susceptibility values are in agreement with the particle material. Thus, the MAP provides a path for in-line rapid quality control assessment of nanoparticles in their final application environment.

I. Introduction

Magnetic nanoparticles (MNPs) have become a crucial nanotechnology tool with wide-ranging applications across medicine,¹⁻⁶ energy,⁷⁻⁹ and environmental sciences.^{10,11} Due to their magnetic response, they can be easily manipulated using external magnetic fields. When combined with a surface functionalization taking advantage of their high surface-area-to-volume ratio, MNPs can

selectively target chemical or biological moieties. As a result, MNPs are particularly effective in nondestructive separation applications, such as cell purification and environmental decontamination. This ability is in direct contrast to many other approaches, such as electrical fields or currents, chemicals, or physical filters, which can have wide ranging side effects on a system.

To assess the effectiveness of a MNP for a given application, there are several intrinsic properties including particle size, magnetic response, and bulk composition. In addition, if a surface coating is involved, the coating properties and its effect on the MNP behavior should also be characterized. Methods to characterize the morphological, chemical, electrical, and optical properties of nanomaterials are standard and commonly performed as part of synthetic reaction validation protocols. To evaluate the magnetic response, the magnetic susceptibility of the MNP should be measured. Magnetic susceptibility quantifies how magnetized the material becomes in response to an external magnetic field, and this metric will predict how effectively a particle or particle suspension can be manipulated by a magnetic field.¹² Many MNPs can exhibit superparamagnetism, indicating that they have an extremely strong magnetic response when an external magnetic field is applied but also do not retain magnetism in the absence of such a field.

Unfortunately, determining the magnetic susceptibility of MNPs currently requires a vibrating sample magnetometer (VSM)¹³ or a superconducting quantum interference device (SQUID)¹⁴. These instruments both perform direct measurements of the magnetic moment, albeit using different mechanisms. Due to the precision required, they are difficult to use, require significant expertise to operate, and are very expensive to both initially purchase and operate.^{12,14,15} Further, researchers need a strong foundation in physics to interpret and analyze the generated data.¹²

An additional limitation is that VSM and SQUID, which both follow the same testing protocols, require mg-quantities of powdered samples for analysis. As a result, they report a bulk measurement on large MNPs aggregates rather than individually suspended MNPs, as MNPs are intended to be used. Further, drying out MNPs can destroy biologically or chemically active surface coatings, permanently changing their performance and rendering them unusable in the target application. In some fields, like biomedical applications, this sample size represents an entire synthetic batch. As a result of these hurdles, the magnetic susceptibility is rarely reported, even for commercially purchased particles. Therefore, a non-destructive method for analyzing magnetic susceptibility of suspended MNPs is critical to improve reproducibility and reliability and implement in-line quality control for this rapidly emerging technology.

Here, we describe the design and validation of a magnetophotometer (MAP) (Fig. 1). This benchtop instrument is capable of non-destructively determining the magnetic susceptibility of MNPs in solution. We detail the theoretical operating principle and the system design of the MAP, and we validate the system using several distinct synthetic batches of iron oxide nanoparticles, comparing the obtained results to SQUID measurements. Lastly, we confirm the non-destructive ability by characterizing Dynabeads, a commercially available MNP, functionalized with streptavidin. This MNP is the industry standard for performing cell separation in protein solutions and blood, but the manufacturer does not report a magnetic susceptibility value. We characterize the susceptibility value in solution and confirm that MAP analysis does not degrade the bioactivity of the surface coating using a series of biotin solutions. Furthermore, the full system design of the

MAP, including 3D-print files, code, and documentation, are published on GitHub to improve access to this crucial quality control measurement.¹⁶

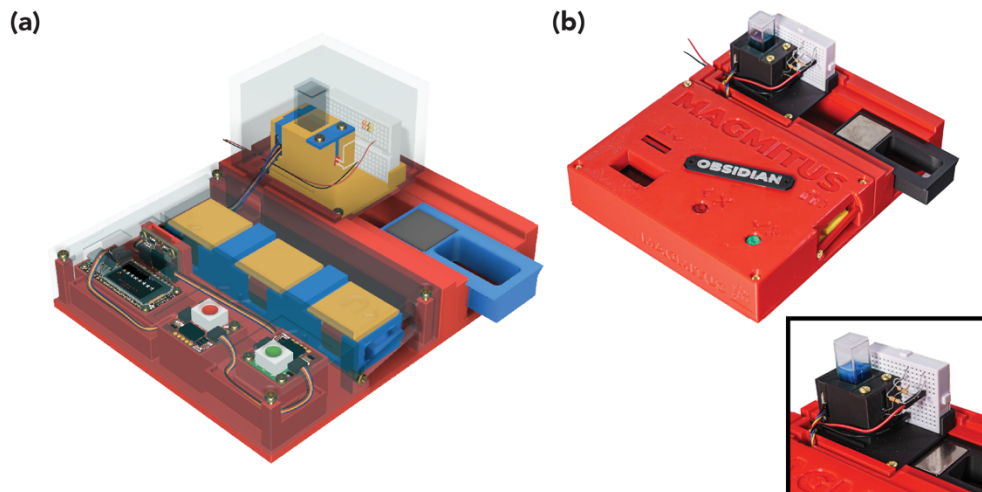


Fig. 1. (a) A rendering of the whole MAP. The opaque covers are shown as transparent to reveal the inner components of the MAP. (b) A photograph of the actual MAP with the cover over the testing stage removed. (inset) A close-up picture of the testing stage.

II. Operating Principle

The detection principle of the MAP is single-wavelength time-dependent differential spectroscopy. Similar to conventional photospectroscopy methods, like UV-Vis spectroscopy, the change in optical intensity as light passes through a sample is measured and correlated to the sample's concentration.¹⁷⁻¹⁹ However, unlike conventional spectroscopy methods, the MAP only uses a single wavelength of light and takes this measurement continuously over time. When the sample is exposed to a magnetic field, the concentration of MNPs in the measurement region decreases as the MNPs are attracted to the magnet and are pulled out of the measurement region. This perturbation of the solution increases the transmitted optical signal, allowing for direct correlation between the optical signal and the movement of the MNPs.

The particle response is governed by parameters intrinsic to the MNP, such as magnetic susceptibility, particle size, and material, and parameters extrinsic to the MNP, such as the solvent viscosity. To use the system to analyze the MNPs' magnetic susceptibility, we derived a mathematical model that relates the light intensity over time to the magnetic susceptibility.

The starting assumption is that an MNP in solution will only experience forces in the z -direction as the magnet is placed directly below the solution. Therefore, the net force F_{net} in the downward direction on an MNP in solution with an applied magnetic field is a combination of the gravitational force F_g , the drag force F_d , the buoyant force F_b , and the magnetic force F_m :

$$F_{net} = F_g + F_d + F_b + F_m. \quad (1)$$

Expanded, this net force can be expressed as

$$F_{net} = mg - 6\pi\eta r\dot{z} - V\rho_s g + \frac{2a^2\chi_p V}{\mu_0(1+\chi_s)}z + \frac{2ab\chi_p V}{\mu_0(1+\chi_s)} + m_0 a, \quad (2)$$

where z and \dot{z} are the position and velocity, respectively, of the particle in the z -direction; m , r , V , χ_p , and m_0 are the mass, radius, volume, magnetic susceptibility, and initial magnetic moment of the particle; η , ρ_s , and χ_s are the viscosity, density, and magnetic susceptibility of the solvent; g is gravitational acceleration; μ_0 is the permeability of free space; and a and b are the geometric and magnetic field parameters, respectively, of a linear approximation of the magnetic field B of a permanent block magnet in the form $B = az + b$.²⁰⁻²²

Using standard differential equation techniques, Eq. (2) can be solved for z to yield an expression for the time-dependent position of a particle in solution:

$$z(t) = k_1 e^{\delta_1 t} + k_2 e^{\delta_2 t} + \frac{\gamma}{\beta} \quad (3)$$

where k_1 and k_2 are unknown constant coefficients and δ_1 , δ_2 , γ , and β are parameters encapsulating the effects of the physical forces.

To more accurately model the physical system, we defined the boundary condition that new particles will not enter the sensing region once the magnetic field is applied. Thus, the number of particles in the sampling region $n(t)$ changes only as function of rate of particles leaving the sampling region:

$$\dot{n}(t) = D\dot{z}(t), \quad (4)$$

where $\dot{n}(t)$ is the rate of change in the number of particles in the sampling region and D is a constant scalar representing the linear density of particles. Solving Eq. (4) for $n(t)$ yields the following time-dependent expression for the number of particles in the sampling region:

$$n(t) = D(k_1 e^{\delta_1 t} + k_2 e^{\delta_2 t} + k_3), \quad (5)$$

where k_3 is a newly defined integration constant.

Eq. (5) can be easily converted to a time-dependent expression for the concentration $c(t)$ (mass/volume) of particles in the sampling region by introducing a scalar factor. In addition, we can apply three boundary conditions: (1) as time increases, the concentration of particles in the sampling region will drop to zero, leading to the elimination of k_3 ; (2) at the initial timepoint, the concentration of particles in the sampling region is some initial c_0 ; and (3) at the initial timepoint, the net velocity of the particles is zero. This yields the final equation:

$$c(t) = \kappa e^{\delta_1 t} + (c_0 - \kappa) e^{\delta_2 t}, \quad (6)$$

where κ is a constant defined in terms of δ_1 and δ_2 . Note that δ_1 and δ_2 are functions of known physical parameters m , η , ρ_p (the particle density), χ_s , μ_0 , and a , as well as two unknown particle parameters: the radius r and magnetic susceptibility χ_p .

The measured light intensity data is converted to concentration via the Bouguer-Beer-Lambert Law²³ and is then fit to Eq. (6), deriving the magnetic susceptibility in SI units. The full derivation of the model and details of the data processing are in the supplementary material.

III. Results and discussion

III.i. System design

The instrument design can be broken into three subsystems: the magneto-optical testing system, the embedded controls system, and the overall packaging into a benchtop instrument. The magneto-optical testing stage was optimized to measure suspended particles in cuvettes. A 620-nm red LED and a light sensor form an optical path through a standard 3.5 mL spectroscopy cuvette. A pinhole restricts the sampling window to a 1 mm x 1 mm region centered around a height of 9.5 mm from the bottom of the cuvette. All components are anchored to a custom baseplate. A labeled schematic of the setup is shown in the supplementary material.

To apply the external magnetic field in a reproducible manner, a manual magnet slider sits on linear slide rails. When the slider is inserted, the neodymium magnet is centered directly below the solution cuvette to apply a magnetic field that varies only in the z -direction. In the current design, the slider is compatible with magnets up to 1" x 1" x 1/2" in size. In this work, the surface field strengths of the magnets ranged from 0 G to 4933 G.

The MAP has an embedded control and data acquisition system with an integrated user interface. The electronics system is built upon open-source hardware and software and requires minimal knowledge of electronics to assemble to increase accessibility.²⁴⁻²⁶ The system is based around a microcontroller with a small display that provides the graphic user interface. The user controls the system using two buttons with integrated LEDs. The microcontroller also collects measurements from the light sensor approximately every 100 ms and records that data on a microSD card for transfer to a computer. All system coding was completed in Arduino C++. This embedded system allows the MAP to run as a standalone benchtop instrument, although data analysis must occur on a computer.

A 3D-printed housing was designed, creating a fully integrated and packaged system with a footprint of about 6" x 7" (Fig. 2). All 3D-printed parts were designed to minimize required support material but still be fully customizable by the user if modifications are needed.

The full details of the MAP design, including a complete bill of materials, assembly instructions, and programming requirements, can be found in the supplementary material. The 3D-printable CAD files and open-source system code are posted on our GitHub.¹⁶

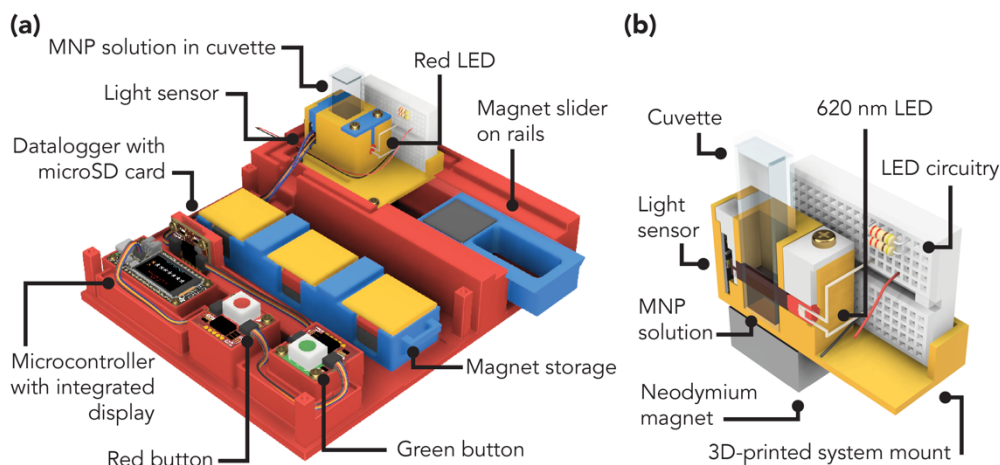


Fig. 2. Labeled renderings of **(a)** the whole MAP with all covers removed for clarity and **(b)** a cross-sectional view of the testing stage.

III.ii. Validation of system performance

After building the system, the MAP's performance was validated through a series of measurements. First, iron oxide (Fe_3O_4) nanoparticles were synthesized in-house three times using a coprecipitation protocol detailed in the supplementary material, creating three distinct batches of MNPs with slightly different properties. The magnetic susceptibility values of these batches were analyzed using both the MAP and commercially available, ultra-sensitive magnetometers. In addition to these tests, we varied both the MNP solution concentration and the magnetic field strength, allowing us to rigorously validate our model. Lastly, using the acquired data, we calculated several classic sensor performance metrics, detailed in the supplementary material.²⁷

Magnetic susceptibility measurements compared to SQUID

To prepare the samples for MAP testing, iron oxide MNPs were suspended in water at a concentration of $100 \mu\text{g}/\text{mL}$. Prior to testing, we ensured each sample was at room temperature to avoid temperature-dependent changes in magnetic susceptibility.¹² Each sample was thoroughly sonicated for at least 5 minutes and vortexed for at least 1 minute to minimize artifacts related to measuring magnetic samples in solution, such as MNP aggregation and settling.²⁸ A volume of 1 mL of solution was added to a standard 3.5 mL spectroscopy cuvette and inserted into the testing stage of the MAP. For these tests, a $1'' \times 1'' \times 1/2''$ N52-grade neodymium magnet with a surface field of 4933 G was applied immediately as data collection began. The time-dependent intensity data was converted to time-dependent concentration and then fit to Eq. (6) to find the magnetic susceptibility. Each sample was tested in triplicate and was resuspended via aspiration with a pipette between trials. In addition, two control measurements were performed: MNPs without the magnet perturbation and the solvent (water) with no MNPs. Additional experimental details and signal processing information are included in the supplementary material.

To confirm the MAP results, a portion of each of the three iron oxide batches were also tested in a SQUID magnetometer. To prepare the samples for SQUID testing, the iron oxide MNPs were dried to a powder. A few mgs of powder (6-17 mg depending on the sample) were inserted into a proprietary sample holder. Eicosane (99%, Alfa Aesar) was melted, inserted into the sample holder until filled, and then allowed to solidify, creating a solid matrix around the iron oxide MNP powder. These samples were then tested on a SQUID magnetometer (Quantum Design MPMS 3) to obtain a magnetic hysteresis curve by completing a 5-quadrant sweep, with minimum and maximum applied magnetic fields of -5000 Oe and +5000 Oe, while measuring the magnetic moment of the sample. The magnetic susceptibility was then derived from the slope of the linear fit of the initial part of the data at low magnetic fields (from 20 to 250 Oe), normalized to the volume of the sample. Details of the analysis processes and the full data, including the hysteresis curves and the linear fits for all samples, are located in the supplementary material.

Representative results from batch 1 of the iron oxide MNPs tested in the MAP, along with the pair of control measurements, are shown in Fig. 3(a). In the solution with MNPs, we observe that the intensity measured through the solution increases immediately when the magnetic field is applied. The signal eventually plateaus when the MNPs are completely removed from the sampling region. This change is also evident upon visual inspection of the cuvette before and after testing (Fig. 3(a) inset). In contrast, when no magnetic field is applied, the intensity increases only slightly over the timeframe of the measurement because the only perturbation to the system is gravity. This signal represents the optical loss of the cuvette, water, and MNPs, providing a lower bound on the measurement signal. In the control with no MNPs, the light intensity does not change, and this signal provides an upper bound on the measurement. As can be observed in Fig. 3(a), the signal from the MNPs with magnetic field perturbation falls between the two control measurements, indicating that the magnetic field removes nearly all the MNPs from the sampling region.

To obtain the magnetic susceptibility, the time-response data was calibrated and fit to Eq. (6). An example of calibrated data and its respective fit is shown in Fig. 3(b). For this specific data set, the predicted magnetic susceptibility is 5.15 and the fit has an r^2 value of 0.987, indicating strong agreement with the theoretical model. All magnetic susceptibilities are reported in SI units. Using this approach, the magnetic susceptibilities for all MNP batches were determined using the MAP, with the results shown in Fig. 3(c). Each measurement replicate is plotted individually and is listed in Table SX in the supplementary material to highlight the reproducibility of the method. The SQUID results are also presented in Fig. 3(c) for direct comparison. Notably, as expected, there are subtle variations in magnetic susceptibility due to the different synthetic batches.^{29,30} These are detected by both the SQUID measurements and by the MAP. These findings are summarized in Table I, which also gives the difference between the MAP and SQUID results.

Crucially, the magnetic susceptibility reported by the MAP falls within the expected range of magnetic susceptibility for magnetite (Fe_3O_4)³¹ and in the same order of magnitude of the SQUID measurements. Despite the slight differences, the magnetic susceptibilities trend in the same direction between both methods, with batch 1 having the highest magnetic susceptibility and batch 3 the lowest. However, it should be noted that the measurement via SQUID provides a bulk measurement on several milligrams of particles fixed in a solid matrix. Because the particles are in close proximity, their dipoles can interact, which could increase the overall magnetic response of

the bulk material.^{32–34} In contrast, the MAP measures magnetic susceptibility of nanoparticles in solution at dilute concentrations, so the interactions between dipoles may be less likely. We would therefore expect MNPs in solution to have a slightly weaker magnetic response and thus a slightly lower magnetic susceptibility than a bulk sample.³³ Therefore, unlike the bulk measurement provided by a SQUID or VSM, a MAP can provide an accurate, more relevant magnetic susceptibility measurement by determining the susceptibility of the particles in solution, which existing magnetometers cannot.

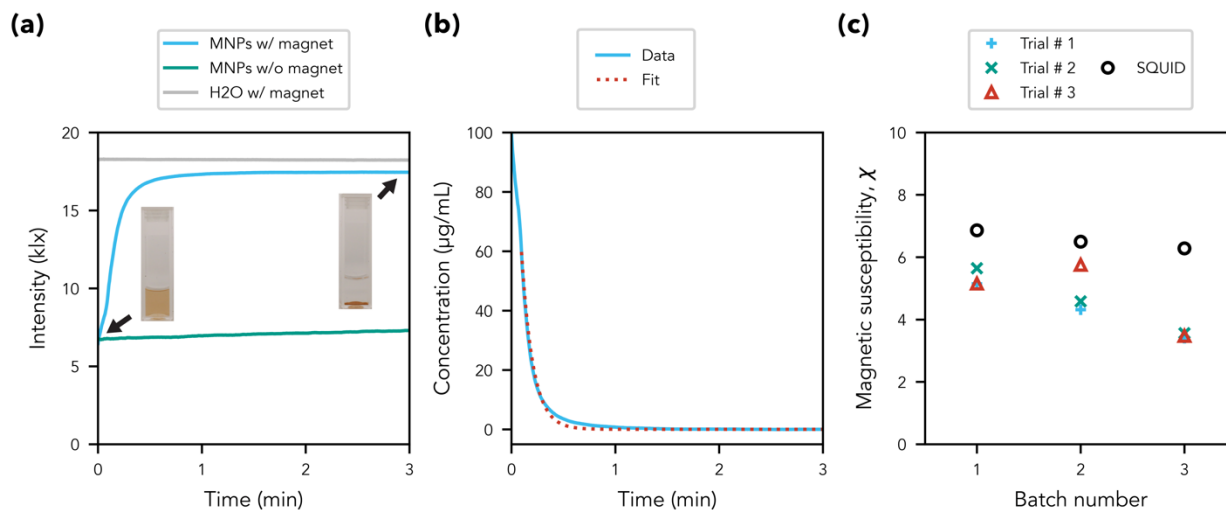


Fig. 3. (a) Raw MAP data from iron oxide MNPs in water (batch 1) tested with an applied magnetic field (blue), iron oxide MNPs (batch 1) in water tested without an applied magnetic field (green), and a control of water tested with an applied magnetic field (gray). (inset) Pictures of the 3.5 mL cuvettes with 1 mL of solution at the beginning and end of MAP testing, corresponding to initial and final concentrations of MNPs. (b) An example of calibrated data and its fit to Eq. (6). The blue line shows the data from part a which has been calibrated and transformed into time-dependent concentration data. The red dotted line shows the fit after data pre-processing, as described in the supplementary material. (c) The magnetic susceptibility of each batch determined from the MAP and the associated SQUID data for that particle batch, reported in SI units.

Table I. Measured magnetic susceptibilities^a of three batches of iron oxide nanoparticles.

Batch No.	MAP χ Average (\pm Std. Dev.) ^b	SQUID χ
1	5.31 ± 0.29	6.86
2	4.88 ± 0.77	6.50
3	3.48 ± 0.08	6.28

a) Reported in SI units. b) Average and standard deviation of the magnetic susceptibility values obtained from three MAP trials of the same sample.

In addition to providing a more relevant single-particle measurement in solution, the MAP has significant advantages relative to a SQUID or VSM. First, it is important to note that the quantity of MNPs required for MAP analysis is less than 0.5 mg. In the series of measurements shown in Fig. 3

and reported in Table I, just 0.1 mg was used. This quantity is an order of magnitude lower than for VSM or SQUID measurements, both of which require a few mg. In addition, when evaluating the base cost of the instrument and the cost per test, the MAP is significantly cheaper than a SQUID, making it a more accessible option to the average researcher. A MAP is a mere \$160 US dollars (USD) relative to the over half a million USD for a SQUID, and a standard spectrophotometry cuvette is 25 times cheaper than the proprietary sample holders required for a SQUID, putting the cost per MAP test on the order of cents. In contrast, a SQUID test requires expensive cryogenic cooling¹⁴ and potentially additional fees for access or staff time. Finally, the analysis of MAP data is straightforward with our provided open-source analysis script unlike analysis of SQUID data, which typically requires significant understanding of electromagnetics.¹² Thus, the MAP, in addition to providing the more relevant measurement of magnetic susceptibility of suspended MNPs, also has significant practical advantages over existing magnetometers that allow the MAP to increase access to these important quality control measurements.

Measurements of varied concentrations

To further validate the system and the model, we tested a range of MNP concentrations from 1 to 500 $\mu\text{g/mL}$ prepared with iron oxide MNPs from synthesis batch 1. The same testing procedure described in the previous section was used, including performing all measurements and all controls in triplicate. Additional experimental details are in the supplementary material.

A subset of MAP data for this series is shown in Fig. 4(a). The full dataset, including data for all concentrations, replicates, and control measurements, can be found in the supplementary material. We observe that both the measured intensity at the beginning of the data collection period and the overall change in intensity observed over the course of the data collection period is proportional to the initial solution concentration, consistent with Beer's law. Once the signal has stabilized, the final intensity measurements should correspond to a solution with no MNPs. For most of the concentrations studied, this boundary condition held true. However, there was one outlier (31 $\mu\text{g/mL}$) that became apparent when the data was analyzed in the intensity-domain and presented as absolute values. This could be attributed to other slight differences, such as scattering related to the positioning of the cuvette within the MAP or fluctuations in the LED power. This outlier emphasizes the importance of analyzing the data in a differential manner and focusing on the change in signal. However, should this become a significant problem in any given MAP instrument, simple modifications to the instrument could be made to correct these changes, as described in the supplementary material.

In Fig. 4(b), the change in intensity across the entire concentration range is presented, and the system exhibits a classic sigmoidal response with both linear sensing and saturation regions. However, before fitting the result to a sigmoidal function, the behavior of MNPs in suspension needs to be considered. One classic property of MNPs is aggregation at high concentrations. When this begins to happen, the fundamental single nanoparticle assumption of our model breaks down, and the sensor response curve deviates. This aggregation point is clearly evident in the data presented in Fig. 4(b) and appears to occur between 125-250 $\mu\text{g/mL}$.

In order to fit the data with a sigmoidal function, we established an upper bound on the change in intensity at high concentrations of approximately 14 klx. Based on the control data, this value represents the maximum theoretical change. Using this approach, we then fit the data to a sigmoid. The linear working range of the MAP fell roughly between 16 $\mu\text{g}/\text{mL}$ to 125 $\mu\text{g}/\text{mL}$, and the system began to saturate around 250 $\mu\text{g}/\text{mL}$, approximately the same concentration that the MNP solutions aggregated. As indicated, these numbers are only valid for the specific components used in our MAP system, and this type of MNPs. However, they provide a guideline to accelerate protocol optimization with other types and batches of magnetic nanoparticles.

The data was analyzed, and the resulting magnetic susceptibilities for the linear working range are shown in Fig. 4(c). The magnetic susceptibility measured by the SQUID for this batch of MNPs is also shown by the dotted line; it should be noted that SQUID data is not concentration-based. Across all concentrations, the MAP measured similar values to the SQUID. Taking a more detailed inspection of the MAP-derived magnetic susceptibility values, we see that there is a slight upwards trend in the measured magnetic susceptibility. Given that it is very reproducible between the three replicates at each concentration, it could be the result of a system limitation, such as detector sensitivity, or it could indicate a change in particle behavior in the suspension. One possibility is that as the concentration increases, the proximity of MNPs to other MNPs decreases, potentially leading to the formation of chains of multiple MNPs. Because the dipoles of individual MNPs in the chain would be aligned, we might expect these chains to have higher magnetic susceptibilities compared to individual MNPs.^{33,34} This concentration-related information could provide additional insight into measurement optimization or synthetic control because many applications are related to suspended particles.

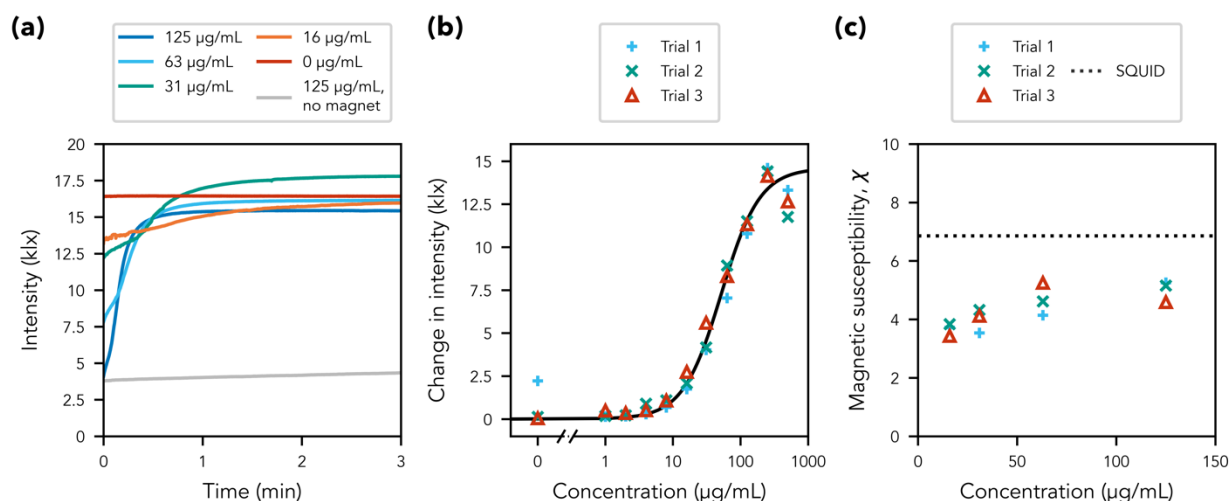


Fig. 4. A sweep of multiple concentrations from 1-500 $\mu\text{g}/\text{mL}$ of a single batch of iron oxide MNPs, tested with the 4933 G surface field magnet. Each concentration was run in triplicate. **(a)** The raw MAP data from the first trial of three selected concentrations, which fall into the linear range for this particle batch, and the first trial of both control measurements: water only (red) and no magnet (gray). **(b)** The sensor response curve showing the measured change in light intensity relative to the initial MNP concentration, fit with a sigmoid function

(black). **(c)** The magnetic susceptibility values determined by the MAP for several concentrations in the working range compared to the value measured by a SQUID. All magnetic susceptibility values are reported in SI units.

Measurements with varied applied magnetic fields

In our theoretical model, concentration and applied magnetic field were the primary variables to control system response. Therefore, in addition to testing with different solution concentrations, we also investigated the role of the magnetic field. Solutions of a single concentration of 100 $\mu\text{g/mL}$ were prepared by suspending iron oxide MNPs from batch 1 in water. These solutions were then tested with 5 different magnetic field strengths in addition to a control of a 0 G field (no applied magnetic field). The surface fields of the 5 applied fields varied from 2108 G to 4933 G. All magnets were neodymium and sourced from K&J Magnetics; the exact magnets are listed in the supplementary material. Note that the surface field of the magnet will be used to refer to the magnets for convenience even though it is not the actual value of the magnetic field strength applied at the sampling window. Each field strength, including the control of 0 G, was used to test the MNPs three times, following previously described protocols.

The first trial for each magnetic field strength is shown in Fig. 5(a). The full dataset, including all three trials can be found in the supplementary material. For all magnetic fields greater than zero, the intensity signal stabilizes to a similar intensity level, which is to be expected because the initial concentrations of the solutions are the same.

To quantify the time-dependent nature of the response on magnetic field strength, we defined the response time as the time it takes for the intensity signal to reach 90% of its maximum change. As can be observed in Fig. 5(b), the response time is directly dependent on the magnetic field strength. This behavior is consistent with the developed model which incorporates the magnetic field strength. A stronger external magnetic field results in a stronger magnetic force, thus corresponding to the more rapid change in signal. Notably, the response time in Fig. 5(b) was less than 60 seconds for all field strengths, which meant that data could be collected for only 3 minutes and still capture the full response with ample margin. This data collection duration was orders of magnitude shorter than the test duration required for VSM or SQUID measurements, which took over 24 hours for a typical test. This difference represents a time savings of 99.8%.

The MAP data was analyzed to derive the magnetic susceptibility values, and the results are shown in Fig. 5(c). The value measured by the SQUID is given by the gray dotted line. It should be noted that the SQUID instrument sweeps over a large range of applied magnetic fields to measure a single magnetic susceptibility, but the value itself is independent of field strength for the relatively low fields used in this work. For all magnetic fields, the magnetic susceptibility derived by the MAP was consistent between trials and agreed with the control values from the SQUID, indicating that our theoretical model correctly modeled magnetic field. Thus, we have demonstrated that the system can be operated either by varying the concentration or the magnetic field strength, providing two modes of operation.

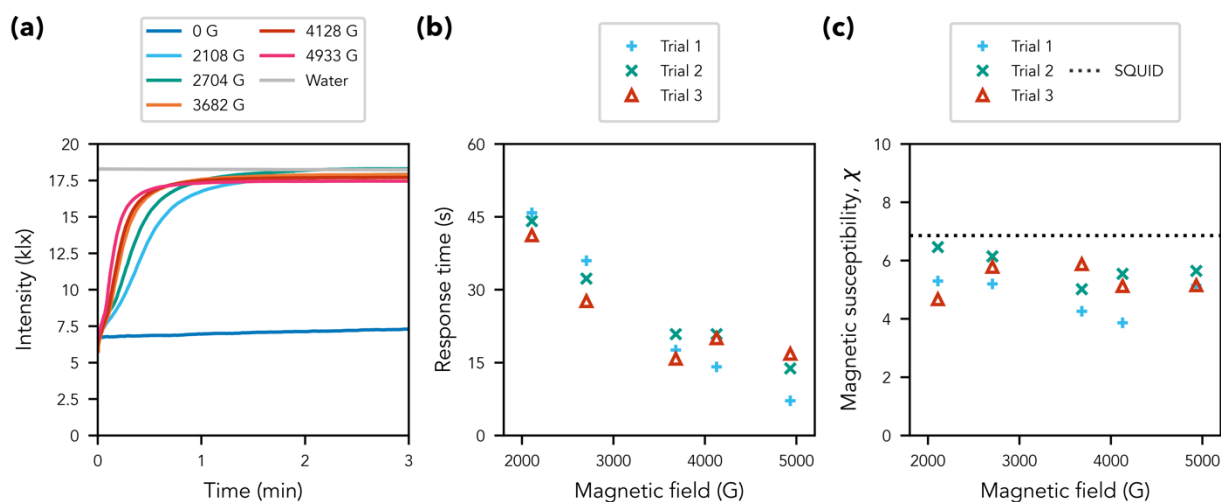


Fig. 5. A sweep of multiple applied magnetic fields on a single batch of iron oxide MNPs, prepared at a concentration of 100 $\mu\text{g/mL}$ in water. Three trials were run at each magnetic field strength, which varied from 0 to 4933 G. **(a)** The raw MAP data from the first trial of all magnetic field strengths, including the control with no magnetic field (dark blue) and with just water (gray). **(b)** The response time (the time for signal to reach 90% of its overall change in value) plotted against magnetic field strength, showing a downward trend in response time as field strength increases. **(c)** The magnetic susceptibility values determined by the MAP for all magnetic field strengths compared to the value measured by a SQUID, reported in SI units.

III.iii. Non-destructive testing of surface-coated MNPs

To confirm that MAP testing does not damage biological surface coatings during a measurement, we analyzed the biological activity and magnetic susceptibility of streptavidin-coated magnetic nanoparticles (ThermoFisher Dynabeads Streptavidin M-280). As a test matrix, we used a series of fluorescein-labeled biotin (fl-biotin, ThermoFisher biotin-4-fluorescein) solutions. The particles were either tested in the MAP or not tested before being used for magnetic sample purification. Both the purification efficiency and the magnetic susceptibility of the Dynabeads were determined.

An overview of the protocol is in Fig. 6(a). Aliquots of Dynabeads were tested in the MAP and then incubated with one of three concentrations of fl-biotin. Three replicates were tested at each concentration of fl-biotin. Then, these tested particles were again tested in the MAP to separate the Dynabeads with any bound, quenched fl-biotin from the solution. Thus, these Dynabeads were tested in the MAP twice (2x MAP). The top of the solution should only contain unbound fl-biotin. Without disturbing the separated Dynabeads, 10% of the sample (100 μL) was extracted from the supernatant at the top of the solution, and the fluorescence of this sample was measured (Molecular Devices SpectraMax M2e). In parallel, the same series of measurements were performed without the initial MAP testing step (1x MAP). The noise level of the fluorometer was assessed using a pair of controls: the solvent alone and the Dynabeads without fl-biotin. As can be

seen in Fig. 6(b), the signal was the same in both control measurements, establishing a noise floor of approximately 2 au.

Independent of number of MAP testing steps, at each fl-biotin concentration, the samples that underwent the Dynabead purification process had statistically significantly reduced fluorescence than the free fl-biotin solutions (Fig. 6(b)). At the two higher quantities of fl-biotin, the fluorescence in the tested Dynabeads samples decreased by an average of 56% and 79% as compared to the control fl-biotin solution. This residual fl-biotin in the tested samples indicated that the streptavidin binding sites on the Dynabeads were saturated, and there were still significant amounts of unbound fl-biotin. In contrast, with the lowest concentration of fl-biotin, we saw fluorescence levels that are similar to the values obtained in the absence of fl-biotin and comparable to the noise floor. This indicated that the Dynabeads have successfully purified or bound the fl-biotin from the sample.

To assess the impact of the MAP testing on the biofunctionalization, we compared the collection efficiency of the tested Dynabeads to Dynabeads that were not exposed to MAP testing *a priori* (Fig. 6(a)). As can be seen in Fig. 6(b), the fluorescence from samples of untested Dynabeads (1x MAP) was less than the free fl-biotin, indicating that the Dynabeads bound fl-biotin and were performing as expected. Additionally, the fluorescence of these samples was not statistically different than that for the samples of tested Dynabeads (2x MAP) at each concentration of fl-biotin, indicating that MAP testing does not affect the Dynabeads' ability to bind proteins and remove them from solution.

Lastly, using the MAP data taken during this measurement series (Fig. 6(a) and Fig. S19), the average magnetic susceptibility value of this batch of Dynabeads was calculated to be 2.63 ± 0.09 , comparable to our previously measured values for iron oxide, the reported magnetic core material in Dynabeads. Notably, other methods of characterizing particles, such as VSM and SQUID magnetometers, require drying the particles and adding an immobilizing matrix to the MNPs during sample preparation. This both destroys the surface coatings of the MNPs and prevents further use of the MNPs. In contrast, the MAP can characterize MNPs in their native environment in a non-destructive manner. For the many commercial MNPs sold with pre-functionalized surfaces for ease of use, the MAP thus provides as a method to perform preliminary quality control measurements prior to using the particles.

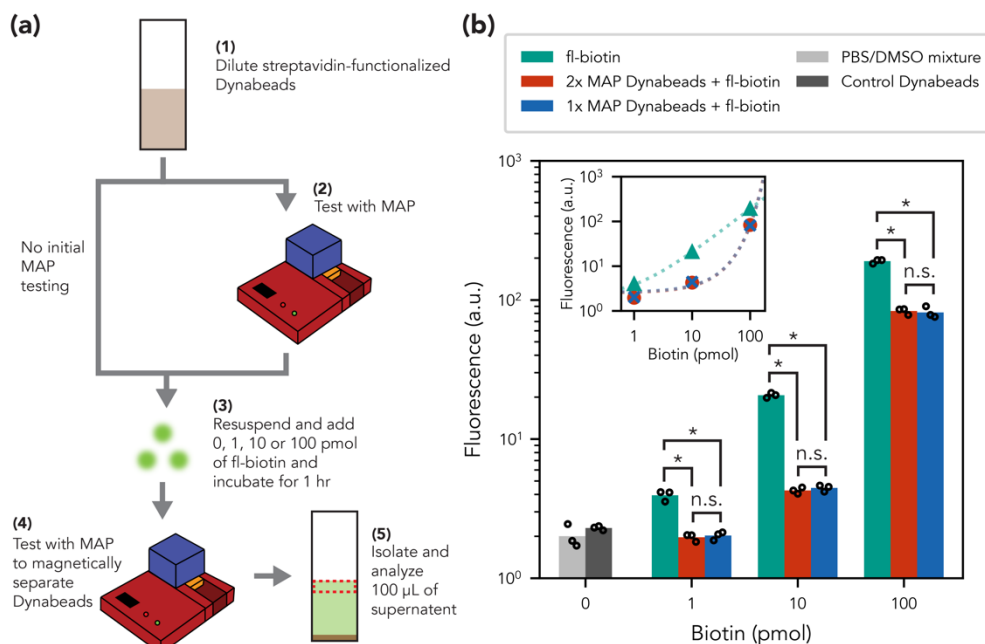


Fig. 6. (a) To confirm that MAP testing does not damage the surface coatings of Dynabeads, 1 mL aliquots of 100 $\mu\text{g}/\text{mL}$ Dynabeads were either tested in the MAP or not tested and then incubated with 1, 10, or 100 picomoles of fl-biotin. All samples were then tested in the MAP to separate the Dynabeads bound to fl-biotin from the free fl-biotin; 100 μL was then removed from the top of each cuvette and the fluorescence at 523 nm was measured (excitation at 494 nm) with arbitrary units (a.u.). **(b)** Average fluorescence of free fl-biotin solutions (teal), the supernatant of 2x MAP tested Dynabeads (red), and the supernatant of 1x MAP tested Dynabeads (blue). Controls of solvent (light gray) and Dynabeads alone (dark gray) were also tested. Student's t-test results: *statistically significant difference between group averages with $p < 0.01$; n.s. no significant difference found. **(inset)** The average at each biotin quantity plotted with a trendline.

IV. Conclusions

We have developed and validated a versatile open-source benchtop MAP that is low-cost and accessible, capable of measuring the magnetic susceptibility of an MNP solution. During system development, we also developed a mathematical model to derive the magnetic susceptibility from the optical measurements. When tested with one of the most common MNP systems, iron oxide MNPs, the results obtained using the MAP compare as expected with the bulk measurements of high-performance SQUID magnetometer and provide a more relevant measurement for most applications of MNPs used in solution. We also confirmed that MAP testing does not damage the performance of biological surface coatings using a standard commercially available particle system, Dynabeads.

The MAP has unique advantages over existing alternatives for magnetic susceptibility characterization. Unlike time-consuming, high-performance SQUID or VSM systems that require milligram quantities of powders embedded in a matrix, the MAP measures magnetic susceptibility of microgram amounts of MNPs suspended in solution within minutes. As a result, the MAP can perform non-destructive measurements on valuable samples in the final application environment

of the MNPs: in solution. By increasing the accessibility to magnetic characterization measurements, the MAP will improve research rigor and commercial product reproducibility by providing scientists with a low-cost and quick method to confirm reagent and material magnetic properties, addressing a pressing need in materials, environmental, and biomedical sciences.

Supplementary Material

The supplementary material includes the full derivation of the theoretical model, a bill of materials, system design details, and assembly and use instructions, as well as the raw data and more detailed analysis than is presented in the main text and the full sensor characterization of the system.

Acknowledgments

The authors would like to thank Armando Urbina, Hari Sridhara, and Ruoqiao Sun for synthesizing the iron oxide nanoparticles used in the performance characterization and validation of the MAP, as well as Kylie Trettner for advice on statistical methods. This project was supported by the Office of Naval Research (Grant No. N00014-24-1-2296), the National Science Foundation (Grant No. DBI-2414158), and The Ellison Medical Institute.

Author Declarations

Conflict of Interest

A.M.A. serves as the Senior Director of Engineering and Physics for Ellison Institute, LLC (paid).

Author Contributions

A.M.A., A.S., and J.P. conceptualized the MAP basis; J.P. and A.S. derived the theoretical model; A.S. and J.P. wrote code to implement the model; A.S. performed validation experiments and data analysis; A.S., J.P., and A.M.A. wrote the manuscript. A.S., A.M.A., J.P., and V.N. edited and approved of the final manuscript documents.

Data Availability

The data that support the findings of this study are available from the corresponding author upon reasonable request. All design materials required to assemble a MAP system, including the embedded system code, the CAD files, 3D print files, and the data analysis program are available at: <https://github.com/armanilab/MAP>.

References

¹ H. Xu, Z.P. Aguilar, L. Yang, M. Kuang, H. Duan, Y. Xiong, H. Wei, and A. Wang, “Antibody conjugated magnetic iron oxide nanoparticles for cancer cell separation in fresh whole blood,” *Biomaterials* **32**(36), 9758–9765 (2011).

- ² Y. Guo, Y. Ran, Z. Wang, J. Cheng, Y. Cao, C. Yang, F. Liu, and H. Ran, “Magnetic-responsive and targeted cancer nanotheranostics by PA/MR bimodal imaging-guided photothermally triggered immunotherapy,” *Biomaterials* **219**, 119370 (2019).
- ³ S. Gandhi, X. Shauli, J. Fock, F. Scheffold, and R. Marie, “IgG and IgM differentiation in a particle-based agglutination assay by control over antigen surface density,” *APL Bioengineering* **8**(2), 026124 (2024).
- ⁴ L. Vítková, N. Kazantseva, L. Musilová, P. Smolka, K. Valášková, K. Kocourková, M. Humeník, A. Minařík, P. Humpolíček, A. Mráček, and I. Smolková, “Magneto-responsive hyaluronan hydrogel for hyperthermia and bioprinting: Magnetic, rheological properties and biocompatibility,” *APL Bioengineering* **7**(3), 036113 (2023).
- ⁵ S. Sepehri, E. Eriksson, A. Kalaboukhov, T. Zardán Gómez De La Torre, K. Kustanovich, A. Jesorka, J.F. Schneiderman, J. Blomgren, C. Johansson, M. Strømme, and D. Winkler, “Volume-amplified magnetic bioassay integrated with microfluidic sample handling and high- T_c SQUID magnetic readout,” *APL Bioengineering* **2**(1), 016102 (2018).
- ⁶ S. Yabukami, T. Murayama, K. Kaneko, J. Honda, L. Tonthat, and K. Okita, “Magnetic response of aggregation mixed with magnetic nanoparticles and protein for simultaneous protein detection,” *AIP Advances* **14**(3), 035102 (2024).
- ⁷ S. Pal, S. Majumder, S. Dutta, S. Banerjee, B. Satpati, and S. De, “Magnetic field induced electrochemical performance enhancement in reduced graphene oxide anchored Fe_3O_4 nanoparticle hybrid based supercapacitor,” *J. Phys. D: Appl. Phys.* **51**(37), 375501 (2018).
- ⁸ J. Zhou, C. Zhang, T. Niu, R. Huang, S. Li, J.Z. Zhang, and J.G. Chen, “Controlled Synthesis of Fe_3O_4 Nanospheres Coated with Nitrogen-Doped Carbon for High Performance Supercapacitors,” *ACS Appl. Energy Mater.* **1**(9), 4599–4605 (2018).
- ⁹ W. Burgess, J. Devkota, and B. Howard, “Wet chemistry-synthesized Fe/mixed ferrite soft magnetic composites for high-frequency power conversion,” *AIP Advances* **14**(2), 025212 (2024).
- ¹⁰ J. Song, F. Zhang, Y. Huang, A.A. Keller, X. Tang, W. Zhang, W. Jia, and J. Santos, “Highly efficient bacterial removal and disinfection by magnetic barium phosphate nanoflakes with embedded iron oxide nanoparticles,” *Environ. Sci.: Nano* **5**(6), 1341–1349 (2018).
- ¹¹ X. Xin, Q. Wei, J. Yang, L. Yan, R. Feng, G. Chen, B. Du, and H. Li, “Highly efficient removal of heavy metal ions by amine-functionalized mesoporous Fe_3O_4 nanoparticles,” *Chemical Engineering Journal* **184**, 132–140 (2012).
- ¹² S. Mugiraneza, and A.M. Hallas, “Tutorial: a beginner’s guide to interpreting magnetic susceptibility data with the Curie-Weiss law,” *Commun Phys* **5**(1), 1–12 (2022).
- ¹³ M. Sundararajan, K. Dahlous, M. Ramesh, R.S.R. Isaac, S. Yuvaraj, J.R. Rajabathar, C.S. Dash, and P.A. Udhaya, “Effect of Al^{3+} substitution on structural, morphological, magnetic, optical, and functional study of ZnFe_2O_4 nanoparticles,” *AIP Advances* **15**(2), 025107 (2025).
- ¹⁴ R.L. Fagaly, “Superconducting quantum interference device instruments and applications,” *Review of Scientific Instruments* **77**(10), 101101 (2006).
- ¹⁵ L. Maldonado-Camargo, M. Unni, and C. Rinaldi, “Magnetic Characterization of Iron Oxide Nanoparticles for Biomedical Applications,” *Methods Mol Biol* **1570**, 47–71 (2017).
- ¹⁶ A. Scholtz, J. Paulson, and V. Nuñez, “Magnetophotometer (MAP) GitHub Repository,” (n.d.).
- ¹⁷ G.F. Lothian, “Beer’s Law and its Use in Analysis,” *Analyst* **88**, 678–685 (1963).
- ¹⁸ S.E. McBirney, D. Chen, A. Scholtz, H. Ameri, and A.M. Armani, “Rapid Diagnostic for Point-of-Care Malaria Screening,” *ACS Sens.* **3**(7), 1264–1270 (2018).
- ¹⁹ S.E. McBirney, K. Trinh, A. Wong-Beringer, and A.M. Armani, “Wavelength-normalized spectroscopic analysis of *Staphylococcus aureus* and *Pseudomonas aeruginosa* growth rates,” *Biomed. Opt. Express* **7**(10), 4034 (2016).

- ²⁰ A.Md.R. Kabir, D. Inoue, Y. Kishimoto, J. Hotta, K. Sasaki, N. Kitamura, J.P. Gong, H. Mayama, and A. Kakugo, “Drag force on micron-sized objects with different surface morphologies in a flow with a small Reynolds number,” *Polym J* **47**(8), 564–570 (2015).
- ²¹ M.A.M. Gijs, “Magnetic bead handling on-chip: new opportunities for analytical applications,” *Microfluid Nanofluid* **1**, 22–40 (2004).
- ²² S.S. Shevkopyas, A.C. Siegel, R.M. Westervelt, M.G. Prentiss, and G.M. Whitesides, “The force acting on a superparamagnetic bead due to an applied magnetic field,” *Lab Chip* **7**(10), 1294–1302 (2007).
- ²³ T.G. Mayerhöfer, S. Pahlow, and J. Popp, “The Bouguer-Beer-Lambert Law: Shining Light on the Obscure,” *ChemPhysChem* **21**(18), 2029–2046 (2020).
- ²⁴ M.D.M. Dryden, R. Fobel, C. Fobel, and A.R. Wheeler, “Upon the Shoulders of Giants: Open-Source Hardware and Software in Analytical Chemistry,” *Anal. Chem.* **89**(8), 4330–4338 (2017).
- ²⁵ D.K. Fisher, and P.J. Gould, “Open-Source Hardware Is a Low-Cost Alternative for Scientific Instrumentation and Research,” *Modern Instrumentation* **2012**, (2012).
- ²⁶ C. Harnett, “Open source hardware for instrumentation and measurement,” *IEEE Instrumentation & Measurement Magazine* **14**(3), 34–38 (2011).
- ²⁷ H.K. Hunt, and A.M. Armani, “Label-free biological and chemical sensors,” *Nanoscale* **2**(9), 1544 (2010).
- ²⁸ Z. Boekelheide, and C.L. Dennis, “Artifacts in magnetic measurements of fluid samples,” *AIP Advances* **6**(8), 085201 (2016).
- ²⁹ I. Nkurikiyimfura, Y. Wang, B. Safari, and E. Nshingabigwi, “Temperature-dependent magnetic properties of magnetite nanoparticles synthesized via coprecipitation method,” *Journal of Alloys and Compounds* **846**, 156344 (2020).
- ³⁰ J. Mohapatra, F. Zeng, K. Elkins, M. Xing, M. Ghimire, S. Yoon, S.R. Mishra, and J.P. Liu, “Size-dependent magnetic and inductive heating properties of Fe₃O₄ nanoparticles: scaling laws across the superparamagnetic size,” *Phys. Chem. Chem. Phys.* **20**(18), 12879–12887 (2018).
- ³¹ B.A. Maher, “Magnetic properties of modern soils and Quaternary loessic paleosols: paleoclimatic implications,” *Palaeogeography, Palaeoclimatology, Palaeoecology* **137**(1–2), 25–54 (1998).
- ³² F. Dinelli, M. Modestino, A. Galluzzi, T. Posati, M. Seri, R. Zamboni, G. Sotgiu, F. Corticelli, and M. Polichetti, “Magnetic Behaviour of Iron Oxide/Dextran Nanoparticles in a Keratin Matrix,” *Applied Sciences* **14**(3), 1106 (2024).
- ³³ V. Reichel, A. Kovács, M. Kumari, É. Bereczk-Tompa, E. Schneck, P. Diehle, M. Pósfai, A.M. Hirt, M. Duchamp, R.E. Dunin-Borkowski, and D. Faivre, “Single crystalline superstructured stable single domain magnetite nanoparticles,” *Sci Rep* **7**(1), 45484 (2017).
- ³⁴ E. Myrovali, N. Maniotis, A. Makridis, A. Terzopoulou, V. Ntomprougkidis, K. Simeonidis, D. Sakellari, O. Kalogirou, T. Samaras, R. Salikhov, M. Spasova, M. Farle, U. Wiedwald, and M. Angelakeris, “Arrangement at the nanoscale: Effect on magnetic particle hyperthermia,” *Sci Rep* **6**(1), 37934 (2016).

Supplementary Material: Open-Source Benchtop Magnetophotometer (MAP) for Characterizing the Magnetic Susceptibility of Nanoparticles

Alexis Scholtz^{1,2}, Jack Paulson^{2,3}, Victoria Nuñez⁴, and Andrea M. Armani^{1,2,3,*}

¹Alfred E. Mann Department of Biomedical Engineering, University of Southern California, Los Angeles, CA 90089, USA

²Ellison Medical Institute, Los Angeles, CA 90064, USA

³Mork Family Department of Chemical Engineering and Materials Science, University of Southern California, Los Angeles, CA 90089, USA

⁴Thomas Lord Department of Computer Science, University of Southern California, Los Angeles, CA 90089, USA

*aarmani@emila.org

I. First principles model derivation

The primary goal of the theoretical model is to develop a mathematical framework to understand how changes in measured light over time caused by magnetic nanoparticle (MNP) motion in a fluid due to a static magnetic field can be used to determine the magnetic properties of the MNP. Specifically, we want to calculate the magnetic susceptibility of our particles, χ_p . Thus, we derived a first principles model, beginning with the forces on a single MNP and then scaling to the multi-particle system present in the MAP (Fig. S1(a)).

I.i. Force on a single particle

We began with a simple free-body diagram of a single particle (Fig. S1(b)). The free-body diagram includes all forces present in the system: buoyancy \vec{F}_b , drag \vec{F}_d , gravity \vec{F}_g , and applied magnetic force \vec{F}_m . The total force that a single particle experiences can thus be written generally as:

$$\vec{F}_{total} = \vec{F}_T = \vec{F}_b + \vec{F}_d + \vec{F}_g + \vec{F}_m. \quad (S1)$$

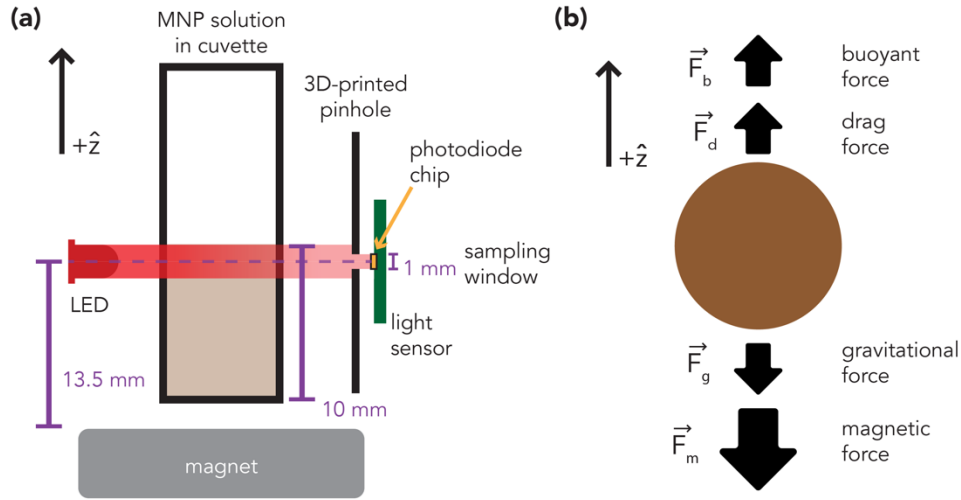


Fig. S1. (a) A simplified schematic showing the testing setup with the optical components and the magnet. Key dimensions are labeled in purple. **(b)** Free-body diagram of all the forces acting on a single nanoparticle.

In the present system, the magnetic force is only applied along the z -axis (Fig. 2, main text). By selecting magnets with a surface (2.54 cm x 2.54 cm) significantly larger than the cuvette (1 cm x 1 cm), any stray magnetic forces due to non-uniformities in the magnet would be uniform in the x - and y -directions. However, the dominant gradient force is in the z -direction. Additionally, given the sensor configuration, the system can only detect changes in z -axis position. Therefore, this expression can be simplified to a single axis (the z -axis). To improve readability, we will drop the vector notation.

The buoyant, drag, and gravitational forces are well defined. The force due to gravity, acting in the negative z -direction, is given by:

$$F_g = -m_p g = -\rho_p V g \quad (\text{S2})$$

where m_p is the mass of the particle, which is equivalent to the density of the particle ρ_p multiplied by the volume of the particle V , and g is the gravitational acceleration. Similarly, the buoyant force is given by:

$$F_b = \rho_s V g \quad (\text{S3})$$

and will act in the positive z -direction on the particle, where ρ_s is the density of the solvent.

The MNPs are assumed to be spherical with diameters with sub-micron diameters. Given the velocities involved, their motion falls in the low Reynolds number regime, and the drag force can be assumed to be Stokes' drag:

$$F_d = 6\pi\eta r \dot{z}, \quad (\text{S4})$$

where η is the dynamic viscosity of the solvent, r is the radius of the particle, and \dot{z} is the velocity of the particle moving in the z -direction.¹ Note even if the particles form chains or cylindrical clumps instead of remaining as spherical particles, Stokes drag will be assumed to apply because of the extremely low Reynolds number. Drag will always oppose overall motion of the particle. In our system, gravitational force will exceed buoyant force because the particles will be much denser

than the solvent and the neodymium magnet will apply a strong downwards magnetic force. As a result, there is a strong net force in the negative z -direction. Thus, we can expect the drag force to be in the positive z -direction.

Therefore, we can write the net force as:

$$F_{net} = \rho_s V g + 6\pi\eta r \dot{z} - \rho_p V g - F_m. \quad (S5)$$

The magnetic force F_m will act in the downwards z -direction towards the magnet. The derivation of the magnetic force is nontrivial and will be discussed in the next section in detail.

I.ii. Magnetic Force

To understand the force acting on a nanoparticle by an external magnetic field, we must first understand how the force relates to the magnetic field. Beginning from first principles, the magnetic force \vec{F}_m by an applied magnetic field \vec{B} on an MNP may be defined as:

$$\vec{F}_m = \vec{\nabla}(\vec{m} \cdot \vec{B}) \quad (S6)$$

where \vec{m} is the magnetic dipole moment of the particle.

Therefore, we need to write an expression for the magnetic moment \vec{m} of the MNP. We also know that the magnetization \vec{M} of the MNP can be defined in two ways:

$$\vec{M} = \frac{\vec{m}}{V} = \chi_p \vec{H} + \vec{M}_0 \quad (S7)$$

where, again, V is the volume, χ_p is the magnetic susceptibility, and \vec{M}_0 is the initial magnetization of the MNP. \vec{H} can be thought of as the auxiliary magnetic field. Note the magnetic field inside the magnet will be neglected because it is irrelevant to this application. Rearranging this equation gives us an expression for \vec{m} :

$$\vec{m} = \chi_p V \vec{H} + V \vec{M}_0 \quad (S8)$$

By defining the initial magnetic moment \vec{m}_0 as $\vec{m}_0 = V \vec{M}_0$, we can simplify this equation to:

$$\vec{m} = \chi_p V \vec{H} + \vec{m}_0. \quad (S9)$$

Note that we do not know \vec{m}_0 . For example, if the particles are superparamagnetic, we can assume that they have no initial magnetization (i.e. $\vec{M}_0 = 0$) and thus no initial magnetic moment (i.e. $\vec{m}_0 = 0$), but to keep this derivation general, we will not make this assumption.

The auxiliary magnetic field \vec{H} must propagate through the solvent to reach the MNPs. To be thorough, we must consider how any magnetization of the solvent may affect the effective magnetic field experienced by the MNP. Assuming that our solvent is a linear media, we can write:

$$\vec{B} = \mu_s \vec{H} \quad (S10)$$

where μ_s is the permeability of the solvent. This permeability can be defined in terms of the permeability of free space $\mu_0 = 4\pi \times 10^{-7}$ as $\mu_s = \mu_0(1 + \chi_s)$ where χ_s is the magnetic susceptibility of the solvent. Thus, we can write:

$$\vec{B} = \mu_0(1 + \chi_s) \vec{H}. \quad (S11)$$

Rearranging Eq. (S11) to write an expression for \vec{H} yields:

$$\vec{H} = \frac{\vec{B}}{\mu_0(1 + \chi_s)} \quad (S12)$$

Substituting Eq. (S12) into the equation for the magnetic moment of the particle Eq. (S9), we get:

$$\vec{m} = \chi_p V \frac{\vec{B}}{\mu_0(1+\chi_s)} + \vec{m}_0. \quad (\text{S13})$$

Returning to our initial definition of magnetic force in Eq. (S6), we can now expand \vec{m} :

$$\vec{F}_m = \vec{\nabla} \left[\left(\frac{\chi_p V}{\mu_0(1+\chi_s)} \vec{B} + \vec{m}_0 \right) \cdot \vec{B} \right] \quad (\text{S14})$$

and distribute the dot product:

$$\vec{F}_m = \vec{\nabla} \left[\frac{\chi_p V}{\mu_0(1+\chi_s)} \vec{B} \cdot \vec{B} + \vec{m}_0 \cdot \vec{B} \right]. \quad (\text{S15})$$

Because the magnetic force only applies in the z -direction, we may simplify and drop vector notation:

$$F_m = \frac{\partial}{\partial z} \left[\frac{\chi_p V}{\mu_0(1+\chi_s)} B^2 + m_0 B \right]. \quad (\text{S16})$$

Note that Eq. (S16) matches the form derived in past work on modeling the magnetic force in paramagnetic MNPs done by Gijs² and superparamagnetic MNPs done by Shevkoplyas et al.³

Now we need to define our applied magnetic field B . The magnets used in the MAP design are block magnets sourced from K&J Magnets, Inc. For this block geometry, the magnetic field in the z -direction at a distance z away from the surface of the magnet is given by:

$$B = \frac{B_r}{\pi} \left[\arctan \left(\frac{LW}{2z\sqrt{4z^2+L^2+W^2}} \right) - \arctan \left(\frac{LW}{2(z+T)\sqrt{4(z+T)^2+L^2+W^2}} \right) \right]. \quad (\text{S17})$$

B_r is the residual flux density, a physical parameter dependent on the grade of neodymium and should be provided by the magnet manufacturer. For two common grades, N42 and N52 neodymium magnets, B_r is 1.32 T and 1.48 T respectively. L , W , and T are the length, width, and thickness, respectively, of the block magnet. In the system, the magnets are oriented such that the thickness is in the z -direction (i.e. the L - W plane is perpendicular to the z -axis).

Eq. (S17) is illustrated in Fig. S2(a). Note that the horizontal axis is the distance z from the surface of the magnet. Furthermore, the light sensor used to collect the light response behavior only integrates over a small sampling window, as indicated in Fig. S1a. In this region, the magnetic field is approximately linear (Fig. S2(b)).

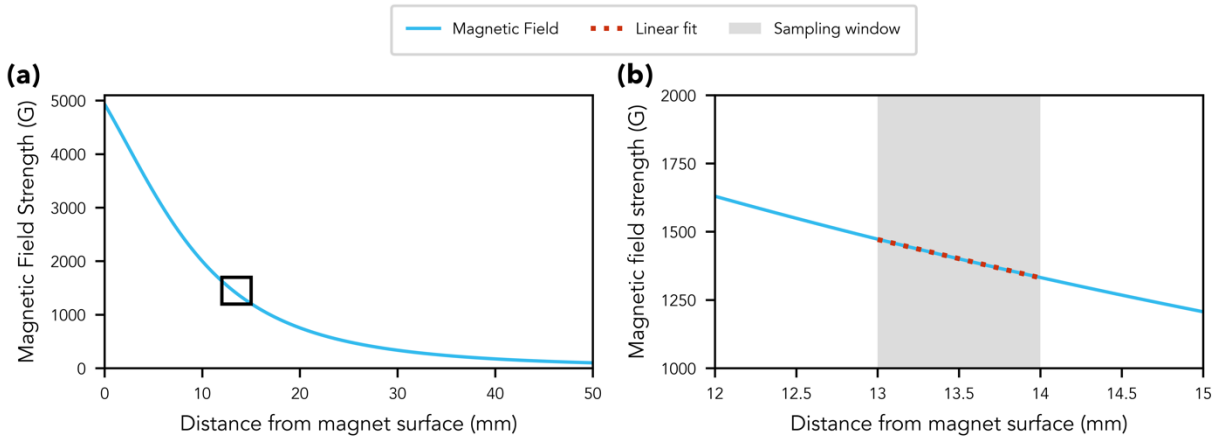


Fig. S2. (a) Magnetic field strength as a function of the distance from the magnet surface. **(b)** The area highlighted in the black box in part a, demonstrating the linear fit of the magnetic field (red dashed line) within the relevant sampling window (gray box).

Thus, the magnetic field in the sampling region can be approximated by a linear equation in the form:

$$B = az + b, \quad (\text{S18})$$

where a and b are the fit parameters that encapsulate the geometric and field parameters of the magnet. In our fit, z is restricted to $z_{bottom} \leq z \leq z_{top}$, where z_{top} and z_{bottom} are the distances to the top and bottom of our sampling region from the center of the L - W plane of the magnet.

Although a quadratic or cubic fit is slightly better at modeling the sampling region of the magnetic field than the linear fit, this would significantly complicate further analysis. We aim to obtain an analytical solution to a second order, nonhomogeneous differential equation, which will be later used to fit experimentally collected sets of data. Therefore, moving forward, we represent the magnetic field with a linear approximation, which proves to be sufficient for our application.

With Eq. (S18) defining the applied magnetic field, we can rewrite the magnetic force expression. From Eq. (S16), we get:

$$F_m = \frac{\partial}{\partial x} \left[\frac{\chi_p V}{\mu_0(1+\chi_s)} (az + b)^2 + m_0(az + b) \right] \quad (\text{S19})$$

Taking the partial derivative and distributing the terms gives:

$$F_m = \frac{2a^2\chi_p V}{\mu_0(1+\chi_s)} z + \frac{2ab\chi_p V}{\mu_0(1+\chi_s)} + m_0 a. \quad (\text{S20})$$

Therefore, Eq. (S20) gives the force an MNP experiences in the sampling window due to a linearly approximated applied magnetic field.

I.iii. Equation of Motion

With the derivation of the magnetic force, we can now write out the full expression for the net force on the MNP in the sampling window:

$$F_{net} = \rho_s V g + 6\pi\eta r \dot{z} - \rho_p V g - \frac{2a^2\chi_p V}{\mu_0(1+\chi_s)} z - \frac{2ab\chi_p V}{\mu_0(1+\chi_s)} - m_0 a. \quad (\text{S21})$$

Using Newton's second law, $F = -m_p \ddot{z}$, with the net force F acting in the negative direction. By substituting $m_p = \rho_p V$, we can arrive at our final net force equation:

$$-\rho_p V \ddot{z} = \rho_s V g + 6\pi\eta r \dot{z} - \rho_p V g - \frac{2a^2\chi_p V}{\mu_0(1+\chi_s)} z - \frac{2ab\chi_p V}{\mu_0(1+\chi_s)} - m_0 a. \quad (\text{S21})$$

Rearranging Eq. (S21) to isolate $\ddot{z}(t)$, we can write it in the standard form of a second order, nonhomogeneous differential equation:

$$\ddot{z} = -\frac{9\eta}{2r^2\rho_p} \dot{z} + \frac{2a^2\chi_p}{\rho_p\mu_0(1+\chi_s)} z + \frac{2ab\chi_p}{\rho_p\mu_0(1+\chi_s)} + \frac{3m_0 a}{4\pi r^3 \rho_p} + \left(1 - \frac{\rho_s}{\rho_p}\right) g. \quad (\text{S22})$$

By defining some additional variables, we can simplify the representation of this equation into:

$$\ddot{z} = \alpha \dot{z} + \beta z + \gamma, \quad (\text{S23})$$

where we define the following:

$$\alpha = -\frac{9\eta}{2r^2\rho_p}, \quad (\text{S24})$$

$$\beta = \frac{2a^2\chi_p}{\rho_p\mu_0(1+\chi_s)}, \quad (\text{S25})$$

and

$$\gamma = \frac{2ab\chi_p}{\rho_p\mu_0(1+\chi_s)} + \frac{3m_0a}{4\pi r^3\rho_p} + \left(1 - \frac{\rho_s}{\rho_p}\right)g. \quad (\text{S26})$$

The α term can be thought of as the drag effects per unit mass, β as magnetic field effects per unit mass, and γ as nonhomogeneous field effects.

The second order, nonhomogeneous form in Eq. (S23) is a commonly solved differential equation and can be found in many math and physics textbooks. The solution yields the equation of motion for a single particle:

$$z(t) = k_1 e^{\delta_1 t} + k_2 e^{\delta_2 t} + \frac{\gamma}{\beta}, \quad (\text{S27})$$

where we define rate-limiting constants δ_1 and δ_2 which encapsulate the drag and magnetic properties of the particle, as:

$$\delta_1 = \frac{-\alpha + \sqrt{\alpha^2 - 4\beta}}{2} \quad (\text{S28})$$

and

$$\delta_2 = \frac{-\alpha - \sqrt{\alpha^2 - 4\beta}}{2}. \quad (\text{S29})$$

I.iv. Relating Equation of Motion to Concentration

If we consider the sampling region to be a single-compartment model, we can write an expression for the number of particles $n(t)$, and ultimately the concentration of particles $c(t)$, within the sampling region at a given point in time. For a single compartment model, we can relate the change of number of MNPs in our sampling region to the velocity of the MNPs by:

$$\dot{n}(t) = D\dot{z}(t), \quad (\text{S30})$$

where D is a constant representing the linear density of MNPs leaving the compartment.

Taking the derivative of Eq. (S27) and substituting it into Eq. (S30) yields

$$\dot{n}(t) = D(k_1\delta_1 e^{\delta_1 t} + k_2\delta_2 e^{\delta_2 t}). \quad (\text{S31})$$

Integrating Eq. (S31) with respect to time to find an expression for $n(t)$ gives us:

$$n(t) = D(k_1 e^{\delta_1 t} + k_2 e^{\delta_2 t}) + k_3, \quad (\text{S32})$$

where k_3 is an unknown constant of integration.

To relate the total number of particles in our sampling region to a concentration (mass per volume), we can divide $n(t)$ by the volume of our sampling window V_w and multiply by the mass of a single particle m_p :

$$c(t) = \frac{m_p}{V_w} n(t). \quad (\text{S33})$$

Expanding $n(t)$ using Eq. (S32) yields:

$$c(t) = \frac{m_p}{V_w} D(k_1 e^{\delta_1 t} + k_2 e^{\delta_2 t}) + \frac{m_p}{V_w} k_3. \quad (\text{S34})$$

We can simplify our expression for $c(t)$ by defining some new constants such that $c(t)$ becomes:

$$c(t) = \kappa_1 e^{\delta_1 t} + \kappa_2 e^{\delta_2 t} + \kappa_3, \quad (\text{S35})$$

where

$$\kappa_1 = \frac{m_p}{V_w} D k_1, \quad (\text{S36})$$

$$\kappa_2 = \frac{m_p}{V_w} D k_2, \quad (\text{S37})$$

and

$$\kappa_3 = \frac{m_p}{V_w} k_3. \quad (\text{S38})$$

Our unknown quantities can be reduced by applying boundary conditions. First, we will apply the boundary condition describing the final state of the system: by the end of the test, there should be no particles in the sample window because they will all be pulled towards the magnet, so the concentration should be zero (i.e. $\lim_{t \rightarrow \infty} c(t) = 0$). Because we have the physical constraints that $\delta_1 < 0$ and $\delta_2 < 0$, the exponential terms of Eq. (S35) should go to 0, and we find that

$$\kappa_3 = 0. \quad (\text{S39})$$

This leaves us with the expression:

$$c(t) = \kappa_1 e^{\delta_1 t} + \kappa_2 e^{\delta_2 t}. \quad (\text{S40})$$

We next apply the boundary condition describing the initial state of the system, when the concentration is a known initial concentration c_0 (i.e. at $t = 0$, $c(t) = c_0$). This yields the following relationship between κ_1 and κ_2 :

$$\kappa_2 = c_0 - \kappa_1. \quad (\text{S41})$$

Finally, we can apply a condition related to the change in concentration over time: at the initial time point, because particles are initially assumed to be at rest, there should be no change in concentration (i.e. at $t = 0$, $\dot{c}(t) = 0$). This yields the final relationship needed to rewrite our system without any integration constants. We can define κ_1 as:

$$\kappa_1 = c_0 \frac{\delta_2}{\delta_2 - \delta_1}. \quad (\text{S42})$$

Using Eq. (S41) and Eq. (S42) and redefining $\kappa = \kappa_1$, we can rewrite Eq. (S40) to yield our final expression for the concentration of particles in our sampling window:

$$c(t) = \kappa e^{\delta_1 t} + (c_0 - \kappa) e^{\delta_2 t}, \quad (\text{S43})$$

where

$$\kappa = \frac{\delta_2}{\delta_2 - \delta_1} c_0. \quad (\text{S44})$$

Based on the physical interpretation of this model in our system, we expect δ_1 and δ_2 to be negative, since the MNPs are attracted to the magnet and thus leaving the sample window. Although δ_1 and δ_2 both encompass many variables, most of the variables are physical constants or parameters that are known. There are just two unknown quantities in this equation: the radius of the particle r and the magnetic susceptibility χ_p .

II. Model Implementation

II.i. Calibration to concentration

When implementing this model to fit the recorded optical signal, the data must be calibrated to transform the data from the measured light intensity to concentration of MNPs in the sampling region. To make this conversion, we take advantage of the temporal nature of the data, which requires that the optical signal plateaued by the conclusion of the data collection. This steady state signal is the equivalent of a blank in UV-Vis spectroscopy. It represents all background signal from the solvent, the cuvette, and any non-magnetic solutes that may be present in the solution since the plateaued signal indicates all magnetic materials have been pulled out of sampling window.

First, the light intensity $I(t)$ is converted to transmission $T(t)$ by using the average of the final 100 data points (approximately 10 seconds) in the steady state signal as the initial light transmission I_0 (the background signal):

$$T(t) = \frac{I(t)}{I_0} \quad (\text{S45})$$

This transmission can then be converted to optical attenuation $A(t)$ via:

$$A(t) = -\log[T(t)] = -\log\left[\frac{I(t)}{I_0}\right] \quad (\text{S46})$$

Based on the Bouguer-Beer-Lambert law (an expanded version of Beer's law to account for both absorption and scattering), attenuation is defined as:

$$A(t) = (\epsilon l + k_{scatter})c(t) + k_{noise} \quad (\text{S47})$$

where ϵ is the molar absorptivity, l is the optical path length, $k_{scatter}$ is a scattering coefficient, $c(t)$ is the time-dependent concentration, and k_{noise} is attenuation related to background species and noise.⁴ To find this linear relationship, we again use the temporal nature of the collected MAP data. The initial point A_0 and the final point of the data A_f correspond to the known initial concentration c_0 of MNPs in solution and a zero concentration MNP solution, respectively. The line fit between these points describes the linear relationship between attenuation and concentration and can be used to transform the time-dependent attenuation $A(t)$ to time-dependent concentration $c(t)$ via:

$$c(t) = \frac{c_0}{A_0 - A_f} \times A(t) + \frac{c_0 A_f}{A_f - A_0} \quad (\text{S48})$$

This concentration time series $c(t)$ found with the transformed data is then fit to Eq. (S43) using nonlinear least squares regression to derive the magnetic susceptibility from the transformed MAP data using the two unknown variables r and χ_p as fit parameters.

II.ii. Data pre-processing

After calibrating the data to a concentration time series, a two-phase regime is commonly observed. The first phase is dominated by random MNP motion introduced into the system via sonication, vortexing, aspiration, or some combination thereof as the MNPs are resuspended. The second phase is dominated by motion induced by forces defined in the mathematical model of the system (i.e. unidirectional motion).

Phase one processes introduce a time delay, which is not fit by the model. This phase change can be determined via an inflection point highlighted in the derivative of the signal. We will discard the initial data as this does not represent the particles' pure response to the magnetic field; the random motion, coupled with the particles' inertia, will delay the uniform response to the forces that are included in the model.

Instead, we will truncate the data at the inflection point and use that as the "initial" timepoint for the start of our model. Fitting our model to the second phase of the response results in more accurate fit implementation. This process is illustrated in Fig. S3.

The discussion justifying this change may be found in the later section discussing the raw data of the multi-magnet measurements.

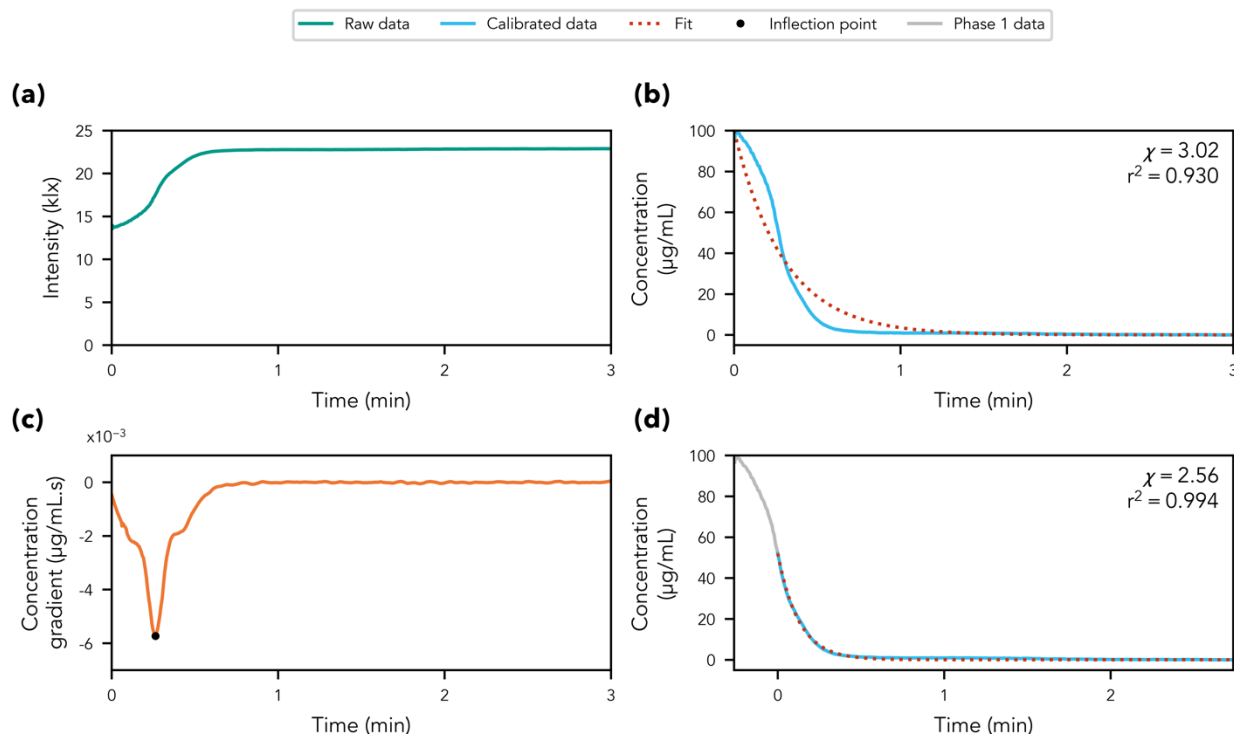


Fig. S3. The pre-processing steps illustrated for the first trial of the Dynabeads MAP tests (section III.iii of main text). **(a)** The raw MAP data (teal). **(b)** The calibrated MAP data (blue) and the fit (red dotted), clearly showing a two-phase response, with the magnetic susceptibility χ and r^2 from the fit. **(c)** The time derivative (orange) of the smoothed concentration data (the blue line in part b), with the inflection point demarcated with a black dot. **(d)** The calibrated data broken into two phases: (1) phase 1 (gray) which is ignored, and (2) phase 2 (blue) which was fit (red dotted) with our theoretical model. The new magnetic susceptibility χ and r^2 value clearly indicating a better fit are shown.

III. Materials and Equipment

The assembly of MAP has three phases: (1) creating the data acquisition path (software), (2) building of the electronics and creating the user interface (hardware), and (3) assembly into the system packaging. Each phase is detailed in the subsequent sections. Full lists of equipment, tools, and materials needed to build this instrument are found in Tables SI-SIII.

From the outset, the MAP was designed to be easy to assemble using readily accessible components. As a result, it does not require advanced equipment or tools beyond access to a consumer-grade 3D printer to create the packaging (Table SI). However, recently, 3D printing services have been established, so direct access to a 3D printer is not even needed.

All hardware materials (Table SII) are widely available from multiple sources; we opted for McMaster-Carr. In addition, all electronics (Table SIII) were selected from companies who follow open-source principles. This philosophy allows greater access to documentation which is critical in the development of a new instrument for a teaching facility as well as broadening potential alternative parts should components become unavailable.

The system is designed to be compatible with any magnets smaller than 1" x 1" x 1/2". We selected a series of N42 and N52 grade neodymium magnets (Table SIV) from K&J Magnetics due to their wide variety, reliability, low cost, and excellent documentation and available resources, including modeling of the magnetic fields. However, the system housing could be easily modified to accommodate additional magnet geometries.

Table SI. Required equipment and tools.

Equipment or Tool	Purpose
3D printer	Produce the custom-designed hardware. Any 3D printer with a minimum layer height of 0.10 mm should suffice, although we used a Prusa i3 MK3S+.
Phillips head screwdriver #1	Insert the #2-56 screws used for securing some of the electronics.
Phillips head screwdriver #3	Insert the #4-40 screws used for securing some of the electronics and hardware.
MicroSD card reader	Connect the microSD card to a computer for data transfer.
5 V USB Power Source	Power the LED and the control system. Note that two USB ports are required.
Xacto knife and/or razor blade	Remove support material and clean up 3D prints if needed (i.e. if there is stringing).
Needle nose pliers and/or flush cutters	Remove support material and clean up 3D prints if needed (i.e. if there is stringing).
Computer with Python 3 installed	Program the embedded system of the MAP and analyze data.

Table SII. Required hardware and materials.

Part name	Vendor	Vendor ID	Cost per unit ^a	Quantity needed	Total cost ^{a,b}
Hatchbox PLA filament ^c	Hatchbox		25.99/kg	549.64 g	14.29 ^d
#2-56 x 3/16" Brass Pan Head Phillips Screw ^e	McMaster-Carr	94070A076	0.063	4	0.25
#2-56 x 3/8" Brass Pan Head Phillips Screw ^e	McMaster-Carr	94070A079	0.082	4	0.33
#4-40 x 1/4" Brass Pan Head Phillips Screw ^e	McMaster-Carr	94070A106	0.084	16	1.34

a) All prices are given by the listed vendor (the source) and are current as of January 2025. Costs shown in US Dollars (USD). **b)** The total cost for all required hardware and materials is \$16.21. **c)** Any standard filament (i.e. PLA, PETG, ABS, etc.) may be used but we experienced smooth printing and sufficient mechanical properties with Hatchbox PLA. **d)** This total cost is estimated based on the amount of filament required to print one full set of the 3D printed parts at the recommended infill percentages given in Table SV. **e)** We recommend brass screws to avoid magnetic interactions with the neodymium magnets but other screws may also be used.

Table SIII. Required electronics.

Part name	Vendor	Vendor ID	Cost per unit ^a	Quantity needed	Total cost ^{a,b}
ESP32-S2 TFT Feather – 4 MB Flash, 2 MB PSRAM, STEMMA QT	Adafruit	5300	24.95	1	24.95
TSL2591 High Dynamic Range Light Sensor – STEMMA QT	Adafruit	1980	6.95	1	6.95
LED – Super Bright Red	SparkFun	COM-00528	1.05	1	1.05
Qwiic Openlog	SparkFun	DEV-15164	18.50	1	18.50
Qwiic Button – Green LED	SparkFun	BOB-16842	4.50	1	4.50
Qwiic Button – Red LED	SparkFun	BOB-15932	4.95	1	4.95
Breadboard – Mini Modular (White)	SparkFun	PRT-12043	4.50	1	4.50
330 Ω Resistor ^c	SparkFun	PRT-14490	0.053	2	0.11
Flexible Qwiic Cable – 100 mm	SparkFun	PRT-17259	1.60	3	4.80
Flexible Qwiic Cable – 200 mm	SparkFun	PRT-17258	1.60	1	1.60
Male-Male Jumper Wires	Adafruit	1956	0.098	2	0.20
SanDisk Ultra 16 GB Micro SD Card ^d	Sandisk	SDSQUAR-016G-GN6MA	6.19	1	6.19
USB Type A to Type C cable (3 ft) ^e	Adafruit	4474	4.95	1	4.95
USB Type A Plug Breakout Cable with Premium Female Jumpers – 30 cm long	Adafruit	4448	1.95	1	1.95

a) All prices are given by the listed vendor (the source) and are current as of January 2025. Costs shown in US Dollars (USD). **b)** The total cost for all required electronics is \$85.20. **c)** A single resistor with a resistance of at least 130 Ω would serve as an alternative. **d)** Any microSD card could be used instead; SparkFun recommends at least a class 6 card for use with the OpenLog. This capacity has proven sufficient to run over 10000 three-minute tests without running out of memory. **e)** This cable will be used to program and power the Feather. The Feather has a Type C connector; the other side may be Type A or C depending on your power source and computer USB ports.

Table SIV. Magnets used in this work.

Part name	Vendor	Vendor ID	Cost per unit ^a	Quantity needed	Total cost ^{a,b}
1" x 1" x 3/16" Nickel Plated (N42) Magnet	K&J Magnetics	BX0X03	5.76	1	5.76
1" x 1" x 1/4" Nickel Plated (N42) Magnet	K&J Magnetics	BX0X04	7.34	1	7.34
1" x 1" x 3/8" Nickel Plated (N42) Magnet	K&J Magnetics	BX0X06	10.51	1	10.51
1" x 1" x 3/8" Nickel Plated (N52) Magnet	K&J Magnetics	BX0X06-N52	13.79	1	13.79
1" x 1" x 1/2" Nickel Plated (N52) Magnet	K&J Magnetics	BX0X08-N52	18.00	1	18.00

a) All prices are given by the listed vendor (the source) and are current as of January 2025. Costs shown in US Dollars (USD). **b)** The total cost for all magnets used in this work was \$55.40.

IV. System Design

The MAP was designed with open-source principles in mind from the start. It has been designed to be easy to operate, easy to assemble, and inexpensive to improve accessibility. The design itself, including editable 3D design files, the code to run the embedded system, and the software to run the data analysis is all published on our Github.⁵ This facilitates modification of the MAP should a user have a specific need for improvement or a new feature.

In this section, we provide an overview of the various hardware components of the MAP: the electronic components and the custom-designed packaging. For the electronic components, we have detailed additional features that were key in the selection of that item. In line with the principles of open-source hardware, we also provide possible alternatives should the specified parts no longer be available or important considerations should the user opt to replace a component with one of their own choosing. For the packaging, we provide print instructions for each of the component files.

We also give an overview of the software design for both the embedded system and the data analysis software. We detail the operation of the MAP and use of the standalone GUI to complete data collection as well as give a brief introduction to the features of the open-source data analysis program that implements our mathematical model.

IV.i. Electronic Components

Based on our overall design constraints, the components all need to be off-the-shelf, inexpensive, and not require soldering. To satisfy this requirement, we chose to utilize I²C communication (Fig. S4), which reduces the complexity of wiring multiple components together, removes the need to solder header pins onto boards, and makes the electronics system much easier to assemble for an inexperienced user. We chose to take advantage of the cross-compatible SparkFun Qwiic and Adafruit STEMMA QT ecosystems. Compatible boards have ports for the 4-wire

cables to be connected serially, and the details of the I²C communication protocols are handled by manufacturer-provided code libraries. The libraries also provide convenient functions for the user to customize code. While modification is not necessary to use our device as initially designed, the open-source nature of both the physical hardware and the software libraries that we chose to employ allows the end user full control of their system should changes be required or other features be desired.

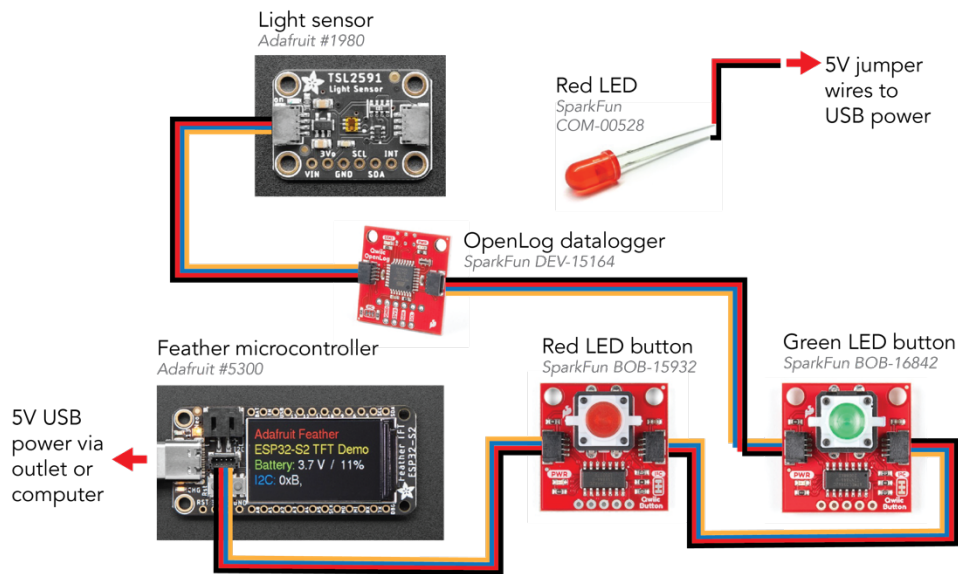


Fig. S4. A schematic showing the wiring between various electronic components and the power sources for each part of the electronics system. Black, red, blue, and yellow lines represent the 4-wire Qwiic cables that connect various boards. The red and black wires to the LED circuit are the +5 V and ground wires. Note that the LED is powered independently from the rest of the electronics, which are powered through shared I²C communication lines.

Microcontroller and Display: Feather ESP32-S2 TFT

The “brain” of the system, the Adafruit Feather, is a microcontroller family built around the open-source Arduino principles. Specifically, the Adafruit Feather ESP32-S2 TFT board (Adafruit #5300), known throughout the rest of the supplementary material as simply the “Feather,” was selected because it boasts both a STEMMA QT I²C port and a built-in TFT display.

The 240 pixel x 135 pixel display is the main output of the MAP’s user interface, which is a crucial component of making the system self-contained. The USB-C port on the board provides power not only to the Feather itself but also to the rest of the components connected via the I²C cables. The Feather is also compatible with both CircuitPython and the Arduino Programming Language. We chose to program the MAP using the Arduino C++ instead of Python to optimize library usage across all the chosen boards and maximize program execution speed to facilitate faster data collection.

It should be noted that this Feather could be replaced by using another Arduino-compatible board, such as a SparkFun Redboard, as long as it is also STEMMA QT- or Qwiic-compatible. If the

microcontroller board does not include a screen, one must be added to allow for a truly embedded system. There is no required screen dimension. However, our code is optimized for the 240 pixel x 135 pixel display found on the Adafruit Feather ESP32-S2 TFT, so a 16:9 aspect ratio would allow for more seamless adaptation of the provided MAP code. The Adafruit ESP32-S3 Reverse TFT Feather (Adafruit #5691) would be an excellent alternative, although it was not available at the time of hardware development for this work, and slight modifications to the 3D-printed base and panel pieces would need to be made for this board.

Light Sensor: TSL2591

There are a wide variety of light sensors available even once I²C compatibility is considered as a filter. We chose the Adafruit TSL2591 (Adafruit #1980) for its high dynamic range and its sensitivity in the visible light region. It has two photodiodes for infrared and full-spectrum measurements that can be used to detect the optical signal. This chip measures intensity values from 188 μ lux up to 88 klux, giving the MAP the capability to measure a wide range of solution concentrations and particle responses to magnetic field application. It also has the option of easily tuning the integration time and the gain of the TSL2591 sensor in the software. After some optimization, these were both set at their minimum values of 100 ms for the integration time and 1 for the gain to maximize the MAP's temporal resolution between measurements and sensitivity.

Alternate options for light sensors include a VEML7700 lux sensor (Adafruit #4162) and BH1750 ambient light sensor (Adafruit #4681), both of which are packaged on the same size breakout board and offer Qwiic/STEMMA QT compatibility, making them straightforward candidates for alternate light sensors that would fit right into the packaging of the MAP. However, we selected the TSL2591 as the superior option for our application.

Light Source: Red LED

Many options are available for light sources. The choice of SparkFun's Super Bright Red light emitting diode (LED) (COM-00528) represented an ideal mix of several factors. First and foremost, red LEDs are cheap as well as reliably and widely available. The wavelength of red light is within the high sensitivity range of the selected light sensor, the TSL2591. The availability of the "super bright" variety from SparkFun increases the maximum power of the LED source without resorting to a laser, which readily saturates the light sensor. By increasing the maximum intensity from the LED, more concentrated solutions may be used in the MAP.

Any infrared or visible LED would work as a replacement should the SparkFun COM-00528 no longer be available. As general design criteria, we suggest selecting a bright LED to maximize compatible concentration ranges. However, we recommend against using a white LED. These are typically made using three separate LEDs (red, green, and blue), which cycle on and off. This could cause small oscillations in the optical signal detected, introducing noise in the data.

A current-limiting resistor must always be placed in series with an LED to avoid damage to the device from over-drawing current (Fig. S5). This resistor value R (in Ohms) can be determined using the following equation derived from Ohm's law:

$$R \geq \frac{V_S - V_{LED}}{I_{LED}}, \quad (S49)$$

where V_S is the voltage supply source in Volts (5 V from a USB supply as designed), V_{LED} is the forward voltage drop of the LED in Volts (2.4 V for SparkFun COM-00528), and I_{LED} is the current through the LED in Amperes (0.02 A or 20 mA for SparkFun COM-00528). We chose to use two 330 Ω resistors in parallel to produce an equivalent resistance of 165 Ω , but any resistor over 130 Ω would suffice for the COM-00528. This simple calculation described by Eq. (S49) should be repeated if a different LED or voltage source is used to select an appropriate current-limiting resistor to avoid damaging the LED.

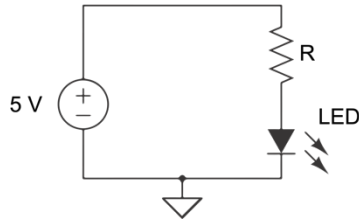


Fig. S5. Schematic of the LED circuit, showing the 5 V voltage source, the resistor (R), and the LED.

Hardware User Interface: Qwiic Buttons with integrated LEDs

Because this system is intended for benchtop use, the development of a fully embedded control and data acquisition system was prioritized. A key element of an embedded system is the user interface that allows the user to operate the system. The user interface of the MAP consists of the TFT display in the Feather as well as two of SparkFun’s Qwiic Buttons, each of which have an integrated LED, one green (SparkFun BOB-16842) and one red (SparkFun BOB-15932). The two buttons form the simplest user interface possible with the capabilities required of the MAP, and the LEDs provide an additional measure of intuitive, instantaneous feedback to the user that the display cannot provide alone.

The Qwiic buttons provided the cleanest packaging for a button and LED. Of course, they could be replaced with individual components and wired using a breadboard.

Data Acquisition: Qwiic OpenLog

The integrated data acquisition system consists of a microSD card and the SparkFun Qwiic OpenLog (SparkFun DEV-15164), which handles writing to the microSD card. The data will be saved in tab-delimited format as a text (.txt) file that can be transferred to a computer for further analysis in a program of the user’s choosing, such as Microsoft Excel or Origin, or via a script written in MATLAB or Python. The OpenLog is capable of writing with speeds up to 20 kilobytes per second, sufficient for use in the MAP.

As an essential piece of hardware in the embedded system, it may prove difficult to replace while retaining I²C compatibility. Adafruit offers a Feather “Wing” capable of writing to microSD cards, but it will require soldering header pins onto the Feather.

IV.ii. 3D-Printed Parts for System Packaging

Files for the system packaging were designed in Autodesk Fusion 360 and are available on our Github repository as both editable .step files and ready-to-print .stl files. Files for the 3D-printed

parts (Table SV) can be found in the zip file named “3D_prints.zip” in the Github repository.⁵ For the 3D printing itself, we chose to use a Prusa i3 MKS3+ 3D printer with Hatchbox PLA filament, but any common filament (i.e. PLA, PETG, ABS) and 3D printer with a minimum layer resolution of at least 0.10 mm and a build volume of at least 150 mm x 180 mm x 33 mm will suffice. All parts were designed without small features and with minimal need for print supports, except as noted. The recommended infill and maximum layer height for each file can be found in Table SV, and the recommended print orientation is shown in Fig. S6. Note that although color of the parts should not matter, we recommend printing the parts in the vicinity of the testing stage in matte black filament to minimize light reflections and scattering that could interfere with measurements; these parts are noted in Table SV.

Table SV. 3D printed parts.

File name	Recommended maximum layer height (mm)	Recommended minimum infill percentage	Print time estimate^{a,b}	Filament estimate^{a,c} (g)
System base	0.20	50%	27h 42m	264.22
Top panel ^d	0.20	50%	7h 56m	93.85
Testing stage ^e	0.10	100%	4h 15m	26.07
Sensor pinhole ^e	0.10	100%	0h 19m	1.65
LED cover ^e	0.10	100%	0h 22m	1.19
Stage cover ^e	0.20	100%	7h 21m	88.18
Magnet slider	0.10	50%	2h 32m	15.50
Magnet storage drawer	0.20	50%	2h 47m	35.06
Magnet storage lid (3 needed) ^f	0.10	100%	0h 33m	3.04
Magnet spacer – 3/16”	0.10	100%	0h 45m	6.39
Magnet spacer – 1/4”	0.10	100%	0h 36m	5.12
Magnet spacer – 3/8”	0.10	100%	0h 20m	2.64
Magnet storage latch	0.20	50%	0h 06m	0.65

a) Print times and filament estimates are based on a Prusa i3 MK3S+ 3D printer with the specified layer height, infill percentage, and orientations given in Fig. S6. **b)** Total print time is estimated to be 56 hours and 40 minutes. **c)** Total mass of filament required is estimated to be 549.64 g. **d)** Supports are recommended for minor elements of this print. Print time and filament estimates both reflect the use of organic supports. **e)** For these pieces which border the optical path and enclose the testing area, we recommend they be printed in matte black filament at full infill to reduce the effects of reflection and scattering. **f)** Note that 3 of these lids are needed to cover all slots in the magnet storage drawer. The individual listed print time and filament estimates are given for one individual magnet storage lid, but the total print time and mass of filament for the full MAP includes all 3 lids.

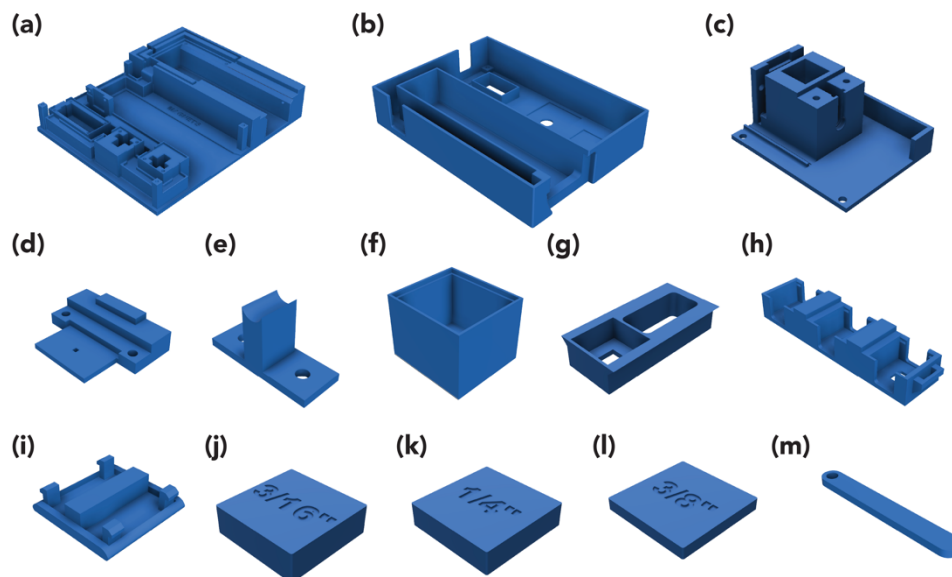


Fig. S6. Print orientations for all 3D printed parts: **(a)** system base, **(b)** top panel, **(c)** testing stage, **(d)** sensor pinhole, **(e)** LED cover, **(f)** stage cover, **(g)** magnet slider, **(h)** magnet storage drawer, **(i)** magnet storage lid, **(j)** magnet spacer – 3/16”, **(k)** magnet spacer – 1/4”, **(l)** magnet spacer – 3/8”, and **(m)** magnet storage latch.

IV.iii. Software Design

We wrote custom, open-source software to complete the embedded data acquisition system on the MAP as well as scripts to visualize and analyze the data, which are all released on the Github repository.⁵ The code running the MAP is written in the Arduino Programming Language and utilizes several libraries released by Adafruit and SparkFun. The program communicates with the hardware, provides a graphic user interface that allows the user to control the system, and collects and saves the data. The MAP data analysis program (MAP-DAP), written in Python, utilizes open-source packages often used in scientific data analysis.

Control System and Graphic User Interface (GUI)

The embedded system is fully coded in Arduino C++. The software of the control system is structured in a state machine to facilitate the user experience, with each state corresponding to a different screen that is displayed on the GUI (Fig. S7) and to different backend functions. These states will be described in more detail, including descriptions of their display and functions, in an effort to describe the control flow utilized by the MAP.

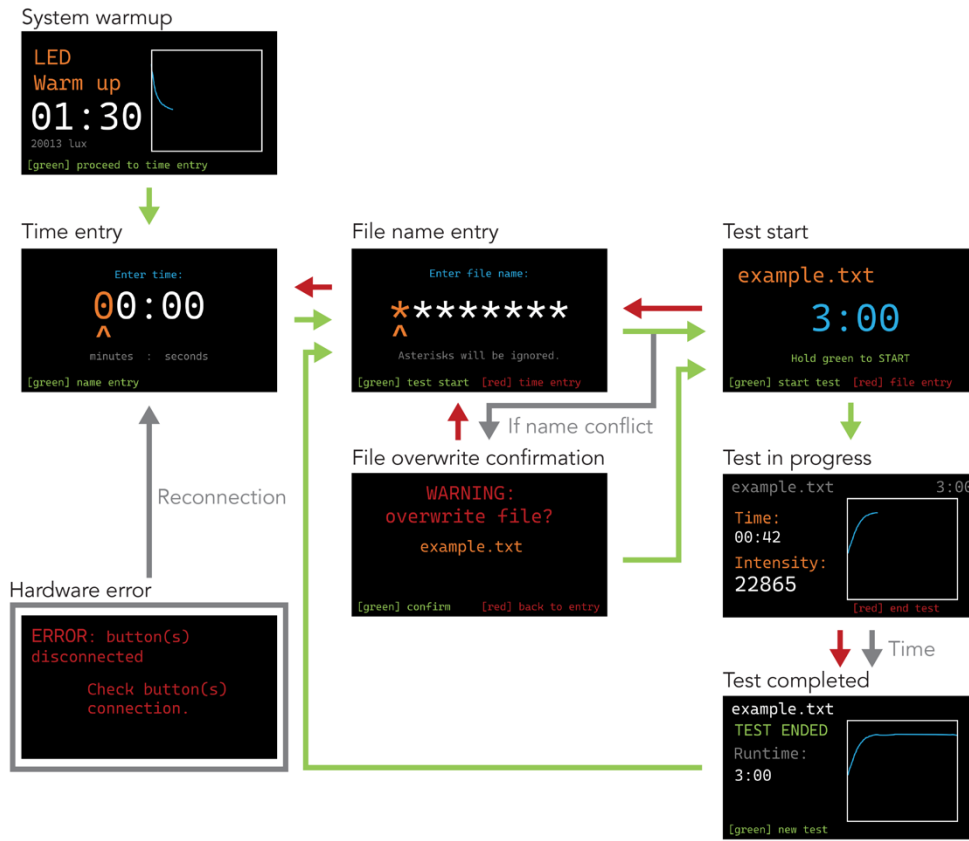


Fig. S7. Renderings of the GUI displays with a simplified control flow shown. A green arrow indicates a long hold of the green button. A red arrow indicates a long hold of the red button. Gray arrows indicate a condition not related to user button presses. The user should hold the green button to proceed with MAP testing after system warmup. The user can navigate through time entry and file name entry by holding the green and/or red buttons. If there is a conflict with the entered file name, the MAP will prompt the user to confirm the file overwrite. Otherwise, the MAP will ask the user to confirm the entered test parameters, and holding the green button will begin the test. During the test, the MAP will display a preview of the data and the current intensity readings, updated approximately every second. At the conclusion of the test, the MAP will show the full data preview and if the user holds the green button, the MAP will reset to file name entry.

User interaction is primarily through the red and green buttons, with any system outputs shown on the display on the Feather. Both buttons have three different selection options based on the length of the button press, which are indicated by the brightness of the LED within the button in real-time. It should be noted that a press is not registered until the button is released. The modes of interaction are summarized in Table SVI but is described in more detail below.

Table SVI. User interaction options.

Description	Duration of button hold (s)	LED behavior	Effect	
			Green button	Red button
Quick click	< 1 s	LED turns on	Increments current selection	Decrements current selection
Short hold	1-2 s	LED flashes once to second brightness level	Advances the selection within the current screen	Returns the selection to the previous one within the current screen
Long hold	> 2 s	LED flashes twice to the third brightness level	Advances to the next screen	Returns to the previous screen

The first option is a quick click, defined as the user holding down the button for less than one second, which will cause the LED in the button to turn on. This quick click is used to increment (green button) or decrement (red button) the currently selected character. The second is a short hold, where the user holds the button down for between one and two seconds and the button flashes once; this interaction option is used to advance the current selection to the next character or return the current selection to the previous character. The third and final option is the long hold, when a button is held down for at least two seconds and will flash twice, getting sequentially brighter. Generally, this long hold will be used to advance to the next screen (if the green button is held) or return to the previous screen (if the red button is held) within the GUI. We have included a visual quick guide that includes the instrumentation controls and the operating process flow as a one-page printable document on our Github.⁵

When the MAP is powered on, the screen will display a timer counting up indefinitely from zero. It is intended to be a timer for the user to allow the LED to stabilize; therefore, it is the user's responsibility to allow sufficient time for the LED to warm up and stabilize prior to taking their readings to avoid introducing artifacts to their measurements. The Troubleshooting section of this document discusses this in more detail. Once the LED signal has stabilized, after about 30 minutes in our experience, the user should execute the long hold on the green button to progress to setting test parameters.

The first test parameter to be set is the test duration. The time is entered in a "mm:ss" format, with a maximum time of 99 minutes and 59 seconds. Using quick clicks of the green and red buttons to increment and decrease digits respectively, and short holds to navigate between the digits, advancing and reversing one selection with the green and red buttons respectively, the user can enter the duration of the test. Once done, the user should perform a long hold of the green button to progress to the file name entry.

Entering the file name is performed in the same manner as setting the time. The file name may be up to 8 characters, which will be appended with ".txt". These characters are initially represented as asterisks but any unchanged asterisks will be removed from the final file name (i.e. an entry of

“test****” will result in a file name of “test.txt”). Character options are the lowercase alphabet, digits 0-9, an underscore, and an exclamation point, in that order. Once the user is satisfied with their entered file name, the user should perform a long hold of the green button to progress to the data collection start. Once entered, the MAP will check to confirm that no file exists on the microSD card with that file name; if there is file of the same name, the MAP will prompt the user to confirm that they want to overwrite the previous file, and if not, will return them to the file name entry screen to modify their entry.

Once the file name has been entered, the screen will display the entered file name and test duration for confirmation. At this point, the sample should be resuspended, inserted into the MAP, and covered in preparation for the test. A long hold of the green button will begin the testing process. The display will prompt the user to push the magnet into place after a 3-second countdown, at which point data collection will begin automatically.

During data collection, the display will show the time elapsed from the beginning of data collection, the current intensity, and a preview of the data. The time and intensity measurements will update every second; the preview of the data will update at intervals corresponding to about every 1/100th of the total test duration to generate the preview of the whole data file (i.e. a 3-minute test would result in points being added to the plot every 1-2 seconds). However, note that the MAP is still logging measurements more frequently, on the scale of 100-150 ms, depending on the performance of the microcontroller. If the user wants to end the test early, a long hold of the red button will end data collection.

When data collection is finished either by completing the full test duration or due to user intervention, the MAP will display the full preview plot and the file name until the user performs a long hold of the green button to return to file name entry. At this point, a new test may be run. Note that the MAP will skip the step of time entry for ease of running consecutive tests, but if the test duration needs to be modified, a long hold of the red button during file name entry will return the MAP to the time entry stage.

If at any point during the use of the MAP, there is a hardware connection error, the MAP will notify the user and prompt them to check the I²C connections between the hardware components. Once connections have been properly re-established, the MAP will return to time entry. Note that if the microSD card is removed from the MAP at any point, the MAP will need to be restarted (i.e. unplugged and powered back on) after the microSD card is re-inserted in order for data to be saved properly.

Data Analysis Program

We implemented the mathematical physics model into a Python script and further developed analysis software to facilitate easier access to magnetic susceptibility measurements by removing the need to rederive the physical mechanism behind our measurement. The MAP Data Analysis Program (MAP-DAP) has a graphic user interface (GUI) coded using the open-source Tkinter library for Python and runs on Python 3. It allows the user to batch select multiple files for visualization and analysis and easily plot the raw MAP data and analyze the files to find the magnetic

susceptibility. MAP-DAP is published on our Github.⁵ There is also a simpler command line version for quick individual file analysis.

V. Assembly Instructions

V.i. Software Setup

Some setup is required before the code can be successfully uploaded to the MAP’s system. The required downloads are summarized in Table SVII. To download and install all software requirements, on a laptop, follow the steps below. This approach is cross-platform and has been tested on Mac OS 14.2 and Windows 11.

Table SVII. Required downloads.

Name	Version ^a	Link
Arduino IDE	2.3.4	https://www.arduino.cc/en/software
ESP32 Package for Arduino Board Manager	3.0.7	https://raw.githubusercontent.com/espressif/arduino-esp32/gh-pages/package_esp32_dev_index.json
SparkFun Qwiic Button Arduino Library	2.0.6	https://github.com/sparkfun/SparkFun_Qwiic_Button_Arduino_Library
SparkFun Qwiic OpenLog Arduino Library	3.0.2	https://github.com/sparkfun/SparkFun_Qwiic_OpenLog_Arduino_Library
Adafruit TSL2591 Library	1.4.5	https://github.com/adafruit/Adafruit_TSL2591_Library
MAP_main	2.0	https://github.com/armanilab/MAP

a) Version used in the MAP. Current as of January 2025.

- 1) Download and install the Arduino IDE if it is not already installed on the computer: <https://www.arduino.cc/en/software>
- 2) For the steps 3-5, follow the instructions given by Adafruit to setup the Feather and Arduino IDE. Major steps are reproduced in brief below, but full detailed instructions can be found at this link: <https://learn.adafruit.com/adafruit-esp32-s2-tft-feather/arduino-ide-setup>
- 3) Set up the Arduino IDE for use with the Feather.
 - a) In the Arduino IDE Preferences, add the following URL to the text field for Additional Boards Manager URLs: https://raw.githubusercontent.com/espressif/arduino-esp32/gh-pages/package_esp32_dev_index.json and click OK to save settings.
 - b) In the Arduino IDE, navigate to Tools > Board > Board Manager, search “esp32,” and click the Install button to install the esp32 package by Espressif Systems.

- c) Plug the Feather into the computer. The computer and Arduino IDE should now recognize the Feather. To confirm, select the Feather as the board by navigating to Board > Adafruit Feather ESP32-S2 TFT.
- 4) Setup and confirm the Feather is ready to be programmed. Major steps are reproduced in brief below, but full detailed instructions can be found at this link: <https://learn.adafruit.com/adafruit-esp32-s2-tft-feather/using-with-arduino-ide>
 - a) The first time the Feather is used, it needs to be placed into ROM bootloader mode. Hold down the DFU/Boot0 button, click the Reset button, and then release the DFU/Boot0 button.
 - b) In the Arduino IDE, navigate to Tools > Port and select the one that says “ESP32S2 Dev Module.”
 - c) To confirm that the Feather is properly setup, open up the Blink sketch from Examples > 01. Basics > Blink and upload it to the Feather. If a warning appears, this is fine and press the Reset button on the Feather. The onboard LED (labeled LED 13) should repeatedly turn on for one second and then turn off for one second.
- 5) Install the Arduino libraries for the TFT display on the Feather. Major steps are reproduced in brief below, but full detailed instructions can be found at this link: <https://learn.adafruit.com/adafruit-esp32-s2-tft-feather/built-in-tft>
 - a) Open the Library Manager from Sketch > Include Library > Manage Libraries...
 - b) Search for “ST7789” and install the Adafruit ST7735 and ST7789 Library.
 - c) Select “Install all” to include all dependencies. If you have not used Adafruit products before, these may include Adafruit GFX Library, Adafruit BusIO, and Adafruit seesaw Library; if you have some or all of these libraries installed already, you may not get this message.
- 6) Install the Arduino libraries for the STEMMA/QT hardware. These are open-source libraries provided by SparkFun and Adafruit that can be downloaded from their respective Github locations. Once downloaded, to install these in the Arduino IDE, navigate to Sketch > Include Library > Add .ZIP Library and select the .zip file for each library. Additional methods to install libraries may be found here if this method does not work: <https://support.arduino.cc/hc/en-us/articles/5145457742236-Add-libraries-to-Arduino-IDE>
 - a) SparkFun Qwiic Button library: https://github.com/sparkfun/SparkFun_Qwiic_Button_Arduino_Library
 - b) SparkFun Qwiic Openlog library: https://github.com/sparkfun/SparkFun_Qwiic_OpenLog_Arduino_Library
 - c) Adafruit Sensor library: https://github.com/adafruit/Adafruit_Sensor
 - d) Adafruit TSL2591 library: https://github.com/adafruit/Adafruit_TSL2591_Library
- 7) Download the MAP repository from: <https://github.com/armanilab/MAP>.⁵ Unzip the file and save the folder at your chosen location. The unzipped directory should be titled “magnetophotometer.” All code can be found in the “code” directory: “MAP_main” contains the Arduino code to run the full MAP system; “hardware_tests” contains code to test various hardware components; and “data_vis” contains the data analysis program.

- 8) Change the I²C address of the green button. By default, both buttons have an I²C address of 0x6F, but to connect both devices simultaneously to the Feather, they must have unique addresses. See Table SVIII for the default and recommended I²C addresses of the various Qwiic/STEMMA QT devices.
 - a) For this step, connect only the green Qwiic button to the Feather. All other I²C devices must be disconnected. Any Qwiic cable may be used.
 - b) In the Arduino IDE, navigate to the magnetophotometer > hardware_tests > change_button_i2c and open change_button_i2c.ino.
 - c) Upload the program to the Feather.
 - d) When prompted, enter “60” to change the I²C address of the green button to 0x60. Confirm that the device address was successfully changed.
 - e) Note that the I²C address may be changed to any other address as long as it is not taken by another device. If another address besides 0x60 is chosen, be sure to change the variable GREEN_I2C_ADDRESS in the MAP_main.ino file to reflect that.

Table SVIII. I²C addresses.

Device	I ² C address
SparkFun Qwiic Red Button	0x6F
SparkFun Qwiic Green Button	0x60 ^a
SparkFun Qwiic OpenLog	0x2A
Adafruit STEMMA QT TSL2591	0x28 and 0x29

a) Changed from default.

- 9) (Optional but highly recommended) Confirm that the libraries and hardware are connected properly by running the following test programs in the hardware_tests folder:
 - a) Open display_testing.ino in the Arduino IDE and upload it to the Feather. The display should turn on and show 3 lines of text: “display test”, “99:99,” and “Hold GREEN to start.” Note that pressing the green button will not actually have any effect.
 - b) Connect both the red and green buttons to the Feather using any Qwiic cables. Open two_button_test.ino in the Arduino IDE and upload it to the Feather. If the buttons are connected and the I²C address has been changed properly, the Serial Monitor in the IDE should say the buttons were connected successfully. When a button is pressed, it should report the button color and whether the button was held for less than one second (clicked), held for one to two seconds (short hold), or held for more than two seconds (long hold).
 - c) Connect the light sensor to the Feather using any Qwiic cable. Open sensor_test.ino in the Arduino IDE and upload it to the Feather. If the TSL2591 is connected properly, the Serial Monitor will confirm successful connection to the sensor and will repeatedly print the lux readings.
 - d) Connect the OpenLog to the Feather using any Qwiic cable. Open openlog_test.ino in the Arduino IDE and upload it to the Feather. If the OpenLog is connected properly, the Serial

monitor will confirm successful connection to the OpenLog and write a file called “test.txt.” to the microSD card. When removed from the OpenLog and connected to the computer, the microSD card should contain a file called “test.txt” containing one line reading “hello world!”

The software setup is now complete; we recommend fully assembling the hardware before continuing with the final program upload.

V.ii. Hardware assembly

An abbreviated set of instructions are included as a one-page printable document on our Github,⁵ but the full assembly instructions are detailed here. We recommend the following order of assembly:

- 1) Print all required packaging parts. See Table SV for the names of individual 3D printed parts with suggested print settings.
- 2) Connect the electronics with the Qwiic cables and orient them properly (Fig. S4).
 - a) Connect a 100 mm Qwiic cable to the Feather and the left port of the red button (when red button is oriented with the text facing the front).
 - b) Connect a 100 mm Qwiic cable to the right port of the red button and the right port of the green button (when oriented with the text facing the front). Turn the green button so that the text now faces away.
 - c) Connect the last 100 mm Qwiic cable to the left port of the green button and the right port of the OpenLog.
 - d) Connect the 200 mm Qwiic cable to the left port of the OpenLog. This will be attached to the light sensor, but for now, leave it disconnected.
- 3) Attach the connected electronics to the system base (Fig. S8(a)). The base should be oriented so that the text embossed into it is readable and facing the front (i.e. towards the user).
 - a) Place the Feather in the bottom left mount in the system base marked with “FEATHER,” oriented so that the USB-C port is on the left side. Attach it with four #2-56 3/16” screws (Fig. S8(b)).
 - b) Place the red button in the square mount marked “R,” oriented so that the two screw holes align with those in the base. Attach it with two #4-40 1/4” screws (Fig. S8(c)).
 - c) Place the green button in the square mount marked “G,” oriented so that the two screw holes align with those in the base. The text should appear facing away from the user, with the green button itself closer to the front of the base. Attach it with two #4-40 1/4” screws (Fig. S8(d)).
 - d) Place the OpenLog in the vertical mount located in front of the text “OPEN LOG”. The board should slide into the opening in the mount, oriented so that the microSD card slot is pointing up. Attach it with two #4-40 1/4” screws (Fig. S8(e)).

- e) (Optional but recommended) Use tape to secure the Qwiic cables in their channels. The 200 mm cable between the OpenLog and the sensor may need to be bundled up to fit nicely.

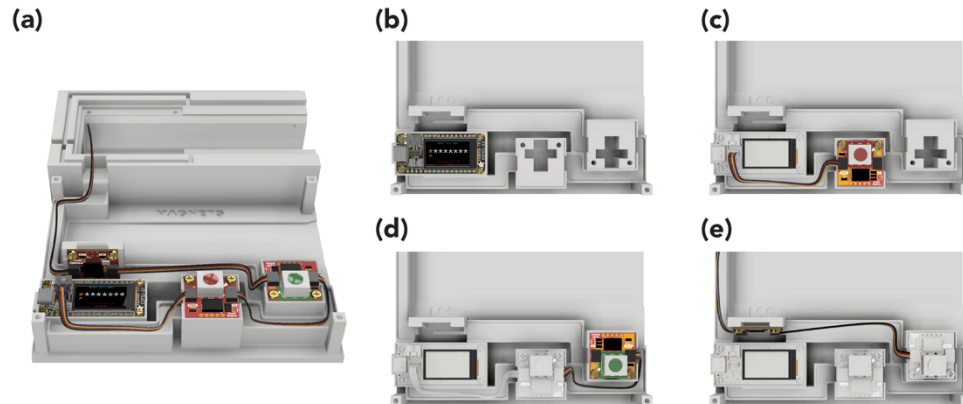


Fig. S8. (a) The MAP fully assembled after step 3, with all electronics secured to the base. All new parts are shown in color. (b) Secure the Feather with four #2-56 3/8" screws. (c) Secure the red button with two #4-40 1/4" screws. (d) Secure the green button with two #4-40 1/4" screws. (e) Secure the OpenLog with two #4-40 1/4" screws.

- 4) Build the LED circuit on the breadboard. See the recommended placement of the components as shown in Fig. S9.
- Place the LED such that the two legs are on opposite sides of the "river" (center division) of the breadboard. This will make it easier to eventually fit the LED into the LED slot of the testing stage in a later step. We recommend placing the longer, positive lead of the LED in breadboard hole 11f and the shorter, negative lead of the LED in breadboard hole 11d.
 - Place two 330 Ω resistors in parallel between the positive lead of the LED and an empty row on the breadboard. We recommend placing the legs of the two resistors in breadboard holes 11j and 15j, and 11i and 15i, respectively. The resistor legs may be trimmed so that the resistors sit lower on the breadboard (as shown in Fig. S9), but it is not necessary.
 - Connect either two jumper wires or two 22 AWG wires with stripped ends to the red and black wires of the USB cable to jumper wire. Insert the jumper wire connected to the red positive wire in the same row as the currently unconnected end of the resistor (row 15), such as in breadboard hole 15f. Insert the wire connected to the black negative wire in the same row as the negative end of the LED (row 11), such as in breadboard hole 11a.

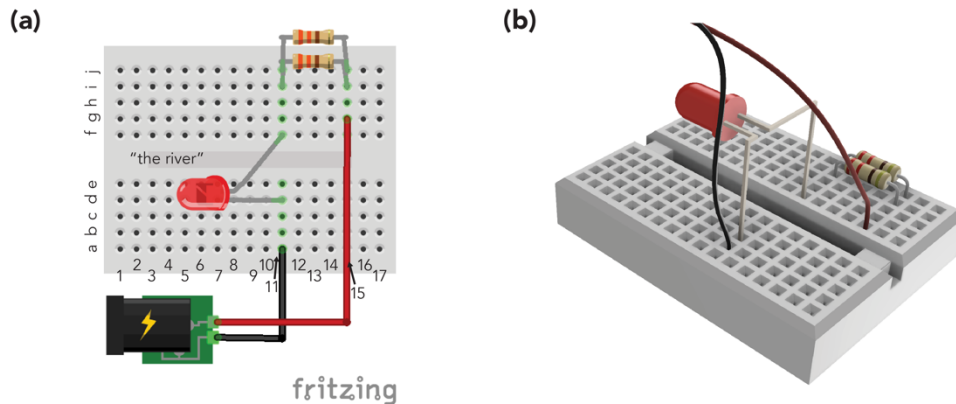


Fig. S9. (a) A schematic of the circuit made in Fritzing and labeled with relevant rows. The green highlights show breadboard rows that are active and connected. **(b)** A rendering of the actual circuit. The red and black wires are the jumper wires, which will eventually be connected to the USB power cord.

5) Assemble the testing stage (Fig. S10(a)).

- a) Slide the TSL2591 light sensor into the slot at the end of the 3D-printed testing stage next to the cuvette holder, oriented so that the text is upright (Fig. S10(b)). Secure the sensor board with two #2-56 3/8" screws slotted through the lower two screw holes of the light sensor and into the bottom two holes of the testing stage (Fig. S10(c)).
- b) Insert the 3D-printed pinhole between the light sensor and the edge of the cuvette holder portion of the testing stage. Note the tab that sits towards the edge of the stage; the top of the pinhole piece should be flush with the top surface of the testing stage. Secure the pinhole with two #2-56 3/8" screws slotted through the top two screw holes of the light sensor, the holes in pinhole, and the top two holes of the testing stage (Fig. S10(d)).
- c) Place the breadboard with the completed LED circuit into the slot along the edge of the testing stage, with the LED sliding down into the bottom of LED slot (Fig. S10(e)). The legs of the LED will need to be bent so that the LED sits at the bottom of the slot.
- d) Place the LED cover into the slot on top of the LED. Use two #4-40 1/4" screws to secure the cover in place (Fig. S10(f)). Note that this piece is not symmetric; it is important that this cover is screwed so that the top is flush against the top surface of the testing stage, which will ensure that the LED is aligned with the TSL2591.
- e) Place the testing stage in the inset at the closed end of the slider rails on the base and secure it with three #4-40 1/4" screws (Fig. S10(g)).
- f) Connect the free end of the 200 mm Qwiic cable from the OpenLog to the port of the light sensor closest to the OpenLog.

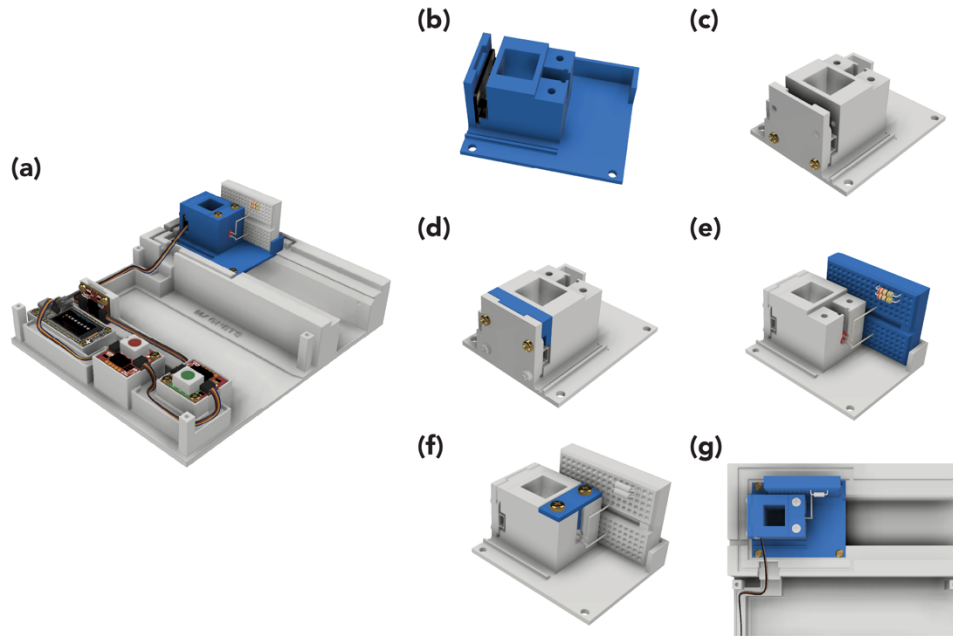


Fig. S10. (a) The MAP as assembled after step 5, with the addition of the testing stage. All new parts are shown in color. (b) Insert the light sensor into the back of the testing stage, oriented right side up (i.e. text is upright). (c) Use two #2-56 3/8" screws in the bottom two screw holes to secure the light sensor. (d) Add the 3D-printed pinhole and secure it with two #2-56 3/8" screws through the pinhole and light sensor and into the testing stage. (e) Add the breadboard with the completed circuit from step 3. The LED legs should be bent so that the LED can slide down to the bottom of the slot. (f) Add the LED cover on top and secure it with two #4-40 1/4" screws. (g) Secure the testing stage to the MAP base with three #4-40 1/4" screws and attach the Qwiic cable from the OpenLog to the light sensor.

6) Assemble the magnet storage drawer (Fig. S11(a)).

- a) For each of the magnet slots, place a magnet and its corresponding spacer into the slot (Fig. S11(b)). Snap the 3D-printed magnet cover into place over the slot (Fig. S11(c)-(d)).
- b) It is recommended to do each slot one at a time to avoid the magnets interacting with each other and to place the spacers on top of the magnets within each slot to minimize potential interactions.

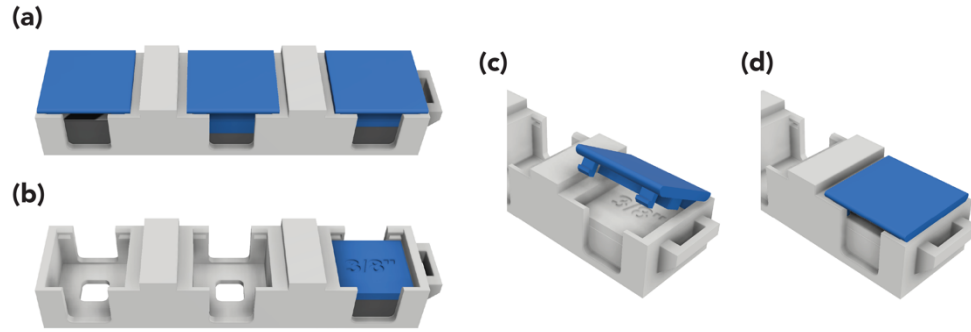


Fig. S11. (a) The magnetic storage drawer fully assembled with lids, spacers, and magnets. (b) It is recommended to place the spacers on top of the magnets to minimize interactions between magnets as much as possible. (c) To insert a lid, place the cantilevers on one side of the lid in their holes in the drawer at an angle and then (d) push the lid down to snap it in place.

7) Assemble the full instrument (Fig. S12(a)).

- a) Use one #4-40 screw to secure the 3D-printed magnet storage latch to the right side of the 3D-printed panel (Fig. S12(b)).
- b) Use four #4-40 screws to secure the panel to the base (Fig. S12(c)). The panel should be oriented so that the openings in the panel align with the microSD card slot of the OpenLog, the screen of the Feather, and the two buttons.
- c) Slide the magnet storage drawer into the MAP (Fig. S12(d)).
- d) Place the removable 3D-printed cover on top of the testing stage so that it rests in the groove around the stage (Fig. S12(e)). Ensure that the jumper wires (LED power wires) emerge from the opening on the left side of the MAP and that the Qwiic cable between the light sensor and the OpenLog sits in the opening entering the panel (Fig. S12(e) inset).
- e) Place the 3D-printed magnet slider in the groove in the rails (Fig. S12(f)). Optionally, a #4-40 screw may be threaded into the hole on the backside of the rails to prevent the slider from being removed from the instrument (for storage purposes only).

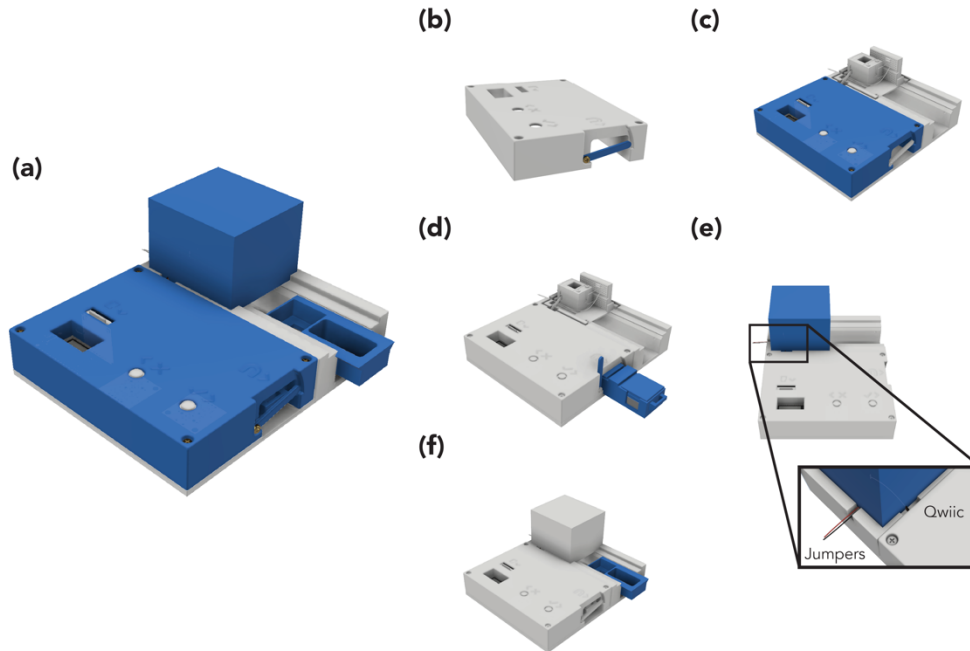


Fig. S12. (a) The MAP fully assembled after step 7. All new parts are shown in color. (b) Attach the magnetic storage latch to the panel using one #4-40 1/4" screw, and (c) then connect the panel to the MAP base with four #4-40 1/4" screws, aligning the openings with the electronics. (d) Slide the magnet storage drawer into its storage location by rotating the latch. (e) Place the cover over the testing stage. (inset) Ensure that the jumper wires and Qwiic cable both sit in their respective channels. (f) Slide the magnet slider into the rails to finish MAP hardware assembly.

V.iii. Final System Programming and Checks

- 1) Set up the MAP for use.
 - a) Insert the microSD card into its slot.
 - b) Connect the two LED jumper wires to the two power wires of the USB-to-jumper-wires cable. The jumper wire connected to the positive side of the LED should connect to the red jumper of the USB cable and the jumper wire connected to the negative side of the LED should connect to the black jumper of the USB cable. The blue and green jumpers of the USB cable will remain disconnected.
 - c) Plug the end of the USB-to-jumper-wire cable into a USB block and plug the USB block into a wall outlet to power the LED.
 - d) Plug the USB-C end of the USB-A-to-C cable into the Feather. Plug the other end into a laptop.
- 2) Upload the MAP code to the Feather and confirm the MAP is assembled properly.
 - a) Open MAP_main.ino in the Arduino IDE.
 - b) Select the Feather board and port and press Upload. The uploading process may take a minute.
 - c) If successful, the screen on the Feather will turn on and begin counting the time since powered on, with the label "LED warming up" (Fig. S7).

- 3) Remove the cover to visually confirm that the LED is emitting red light while the MAP is powered on.
 - a) If it is not, it is likely that the LED is backwards in the circuit. Because LEDs are polarized components, the long leg must be on the positive side (on the side of the +5 V connection) and the short leg on the negative side (on the side of the ground connection). If the LED is not lighting up, try switching the orientation of the LED within the circuit. If the LED still is not lighting up, check that the breadboard circuit was wired correctly.
- 4) Check that the TSL2591 is oriented correctly. The measured lux values reported on the screen should be around or above 15000 lux.
 - a) If lux values are lower than that (i.e. below 5000), the TSL2591 should be removed and turned 180 degrees so that the text on the board is facing up when the TSL2591 is replaced in the stage (Fig. S10(b)).
- 5) Try running a sample test, either with a cuvette filled with water or with no sample at all. Note that if you insert a cuvette of water, the measured lux value may increase.
 - a) Confirm that the microSD card was inserted prior to the MAP being turned on. If not, insert the microSD card; then unplug and power on the MAP again.
 - b) Set the test name and desired time. A short test (for example, 15 seconds) will be fine.
 - c) Start the test and push the magnet in.
 - d) Allow the test to finish. Turn the MAP off and remove the microSD card.
 - e) Copy the file from the microSD card to a computer and view the text file. Confirm that the data was recorded properly. Be sure to insert the microSD card back into the MAP before it is powered on.
- 6) Congratulations! Your MAP system is now up and running properly. Please note the following points regarding MAP operation:
 - a) Once the code has been uploaded, the MAP may be fully powered from a wall outlet.
 - b) The microSD card must be inserted prior to the Feather being powered on for data to be recorded properly.
 - c) The LED needs time to warm up so that the incident light intensity stabilizes prior to testing. The listed SparkFun LED in the bill of materials requires an approximately 30-minute warmup period. See the Troubleshooting section for more information.
 - d) Note that if the microSD card must be removed between tests, the Feather must be restarted once the microSD card is reinserted. Note that this can be accomplished without turning off the LED by removing and reconnecting the USB-C cable from the Feather (to avoid the need for the LED to warm up a second time).
 - e) Do not use too much force when pushing the magnet slider into place; it might cause vibrations that will cause artifacts in the data.
 - f) When setting the test length, it must be long enough for the optical signal to plateau. Since this varies based on factors such as nanoparticle size, nanoparticle magnetic susceptibility, and solvent viscosity, we recommend running a few initial tests to determine the required minimum test duration. Fifteen minutes proved to be more than sufficient as a pilot trial for our iron oxide nanoparticles suspended in water.

- g) We recommend removing the magnet storage compartment from the MAP prior to testing to avoid unintentionally introducing additional external magnetic fields to the measurement stage.
- h) When adding or removing magnets in the storage drawer, we recommend being careful to only remove one cover at a time and keep the magnets themselves far away from each other until actively storing them. They will snap together rapidly, which can be a safety hazard or potentially break the magnets themselves.
- i) We recommend storing the magnets with the plastic spacers on top of the magnets to avoid or minimize potential interactions when adding or removing magnets from the other slots.
- j) The MAP can be sensitive to vibrations; we recommend not running equipment that can produce significant vibrations (i.e. a vortexer or centrifuge) on the same bench during data collection.

VI. Validation Data

VI.i. Iron Oxide Nanoparticle Synthesis Protocol

Iron oxide (Fe_3O_4) nanoparticles were synthesized using a coprecipitation protocol under argon. First, purge the Schlenck line with argon; it is important there is no oxygen in the system to avoid oxidizing the iron chloride precursors. Add 20 mL of deionized (DI) water to the reaction flask, seal with a rubber septum, and turn on the condenser. Using a needle through the septa, purge the flask with argon. In a glove box under argon, measure out 1 g of iron(II) chloride and 0.4 g of iron(III) chloride. Remove the argon and exhaust needles and attach argon to the top of the condenser. Quickly remove the rubber septa from the reaction flask and add the solid iron chlorides before replacing the septa.

Heat the iron chloride precursors and water solution to 80°C on a hot plate. Add 5 mL of ammonia hydroxide dropwise while increasing the speed of the stir bar to prevent the reaction from occurring on the stir bar. Ice should be added to the water tank of the condenser and the argon line removed and replaced with foil over the condenser. Let the reaction occur for 1 hour.

After 1 hour, remove foil from the condenser and open the rubber septa, leaving the flask open to cool. The thermometer and condenser can be removed when cool, and a strong magnet should be used to remove the stir bar from the reaction flask. Then, use a magnet to collect the particles at the bottom of the reaction flask, and when the water is clear, remove the supernatant, using the magnet to retain the particles. Repeat 3 times to wash the particles, adding DI water to resuspend the MNPs each time. Then, add a small volume of DI water to the particles to resuspend and use a Pasteur pipette to remove the particle solution for storage. The particles may also be dried and stored as a powder.

VI.ii. SQUID and VSM Magnetometry

To confirm the validity of our theoretical model, we compared the analyzed data from the MAP to the magnetic susceptibility value obtained from two commercial magnetometers using MNPs from the same synthesis batch. The same samples were tested on both a vibrating sample magnetometer (VSM) and a superconducting quantum interference device (SQUID) magnetometer. Both the sample preparation, testing protocol, and analysis steps are the same for both the VSM and SQUID magnetometers; they vary only in their mechanism to sense the magnetic moment of the sample. The SQUID used was a Quantum Design MPMS 3 at the University of California Santa Barbara Materials Research Laboratory TEMPO Facility and measurements were performed by their staff scientists. The VSM used was a Quantum Design Physical Property Measurement System (PPMS) DynaCool located at the University of Southern California, and measurements were performed by the authors.

To prepare the samples for both magnetometers, the iron oxide MNP solution was fully dried until it was a powder. A plastic sample holder was filled with several mg of powder, just below the halfway point of the holder. The exact mass of iron oxide in the samples prepped from each of our three batches is given in Table SIX. Eicosane (99%, Alfa Aesar) was heated beyond its melting point, until liquid. The remainder of the holder was filled with melted eicosane, the holder was capped, and any residual eicosane cleaned off the outer surfaces of the holder. The eicosane was allowed to cool and set to form a matrix around the iron oxide powder, securing it in place. This prevented the particles from moving within the sample chamber, which would introduce artifacts into the measurements.

The sample was loaded into the magnetometer. The magnetometer carried out a 5-quadrant sweep, applying magnetic fields from 0 Oe, +5000 Oe, -5000 Oe, and finally back to +5000 Oe at a set temperature of 293 K to acquire a magnetic hysteresis curve. A measurement point was taken at a resolution of approximately every 8 Oe change in applied magnetic field. The same protocol was run on both the SQUID (Fig. S13) and VSM (Fig. S14). It should be noted that batch 3 could not be run on the VSM due to an inability to access the VSM when the lab owning the instrument relocated to a different institution. Each sample was only run once due to the high cost of a single measurement session.

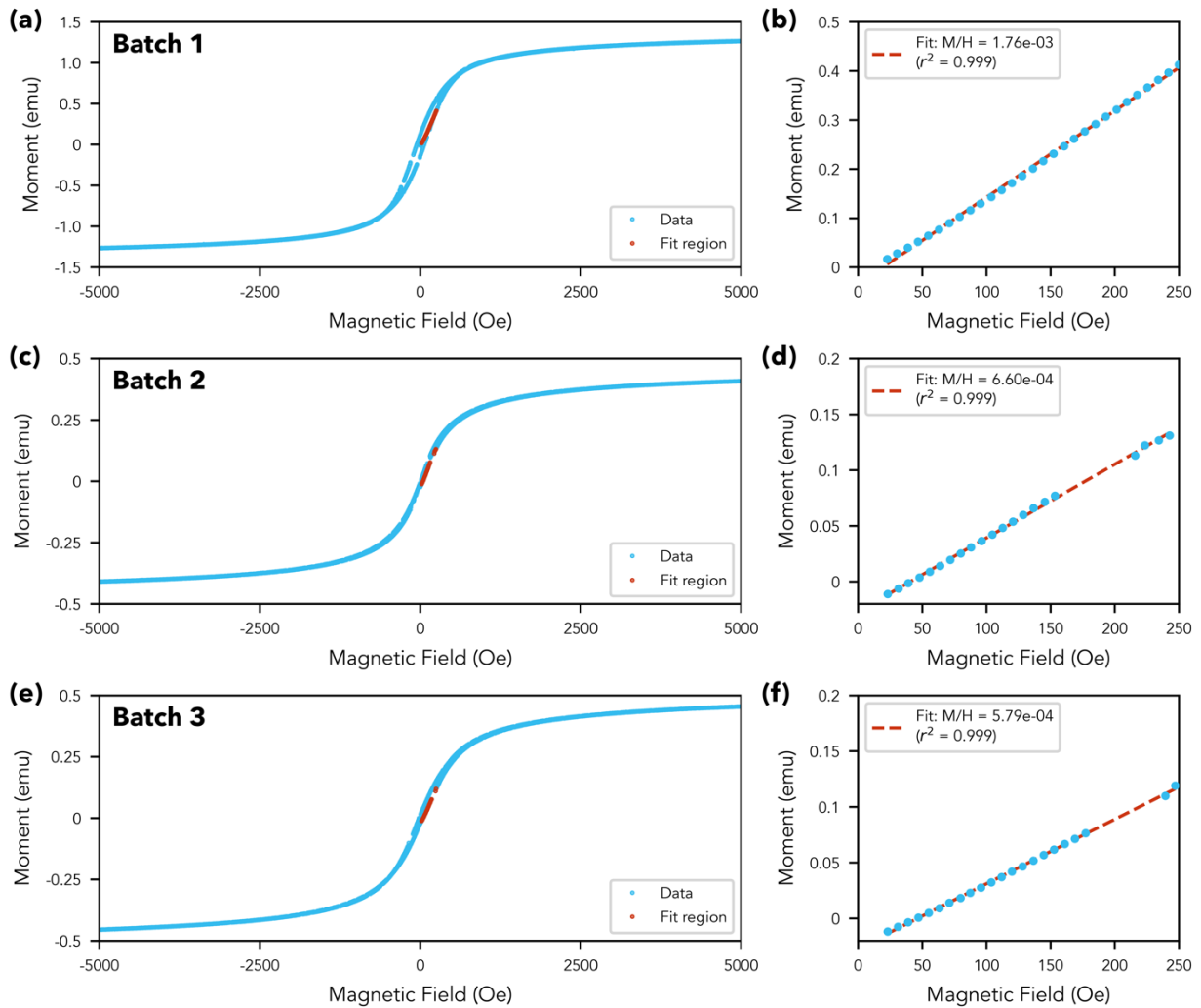


Fig. S13. (left) SQUID data showing the 5-quadrant sweep over a range of applied magnetic field from 0 Oe, to 5000 Oe, to -5000 Oe, and back to 5000 Oe. Data was taken on a Quantum Design MPMS 3. All MNPs showed the expected hysteresis behavior. **(right)** To get the magnetic susceptibility, a line is fit to the initial linear portion when the magnetic field is first applied (shown in red). The slope of that linear fit is the ratio of the magnetization M to the applied magnetic field H . **(a)** Batch 1 hysteresis curve and **(b)** linear fit. **(c)** Batch 2 hysteresis curve and **(d)** linear fit. **(e)** Batch 3 hysteresis curve and **(f)** linear fit.

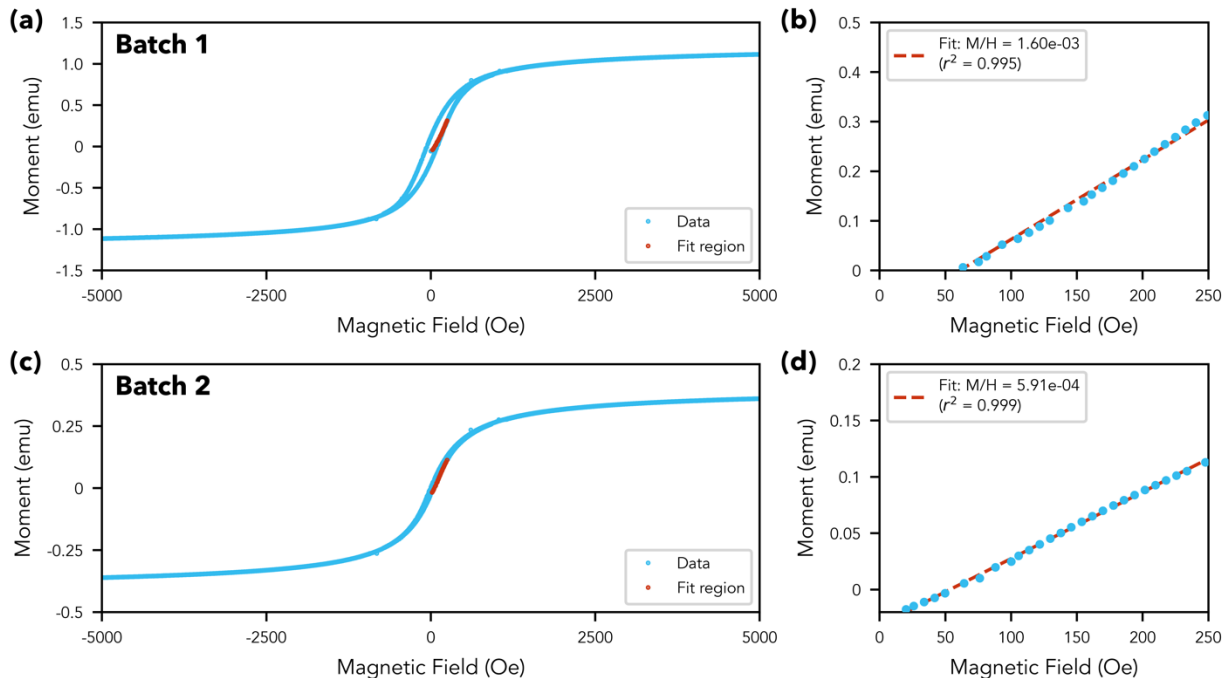


Fig. S14. (left) VSM data showing the 5-quadrant sweep over a range of applied magnetic field from 0 Oe, to 5000 Oe, to -5000 Oe, and back to 5000 Oe. Data was taken on a Quantum Design Dynacool Physical Property Measurement System (PPMS). All MNPs showed the expected hysteresis behavior. **(right)** To get the magnetic susceptibility, a line is fit to the initial linear portion when the magnetic field is first applied (shown in red). The slope of that linear fit is the ratio of the magnetization M to the applied magnetic field H . **(a)** Batch 1 hysteresis curve and **(b)** linear fit. **(c)** Batch 2 hysteresis curve and **(d)** linear fit.

To find the magnetic susceptibility, the linear portion of the curve was fit to a line using standard linear regression techniques. The slope of that linear fit gives the ratio of the magnetization M relative to the applied magnetic field H . For consistency, the linear region was selected to be the portion between 25 to 250 Oe for each sample, and the results had high goodness of fits with each linear model (Fig. S13(b), (d), and (f), and Fig. S14(b) and (d)).

Magnetic susceptibility is typically defined as the magnetization M per unit volume V divided by the ratio of the applied magnetic field H . We converted our measured sample mass to appropriate units of volume using the density of iron oxide. Magnetic susceptibility was calculated in both CGS units, consistent with the units reported by the magnetometers, and SI units, consistent with the units used in our theoretical model derivation. This conversion between the two unit systems is simply:

$$\chi_{SI} = 4\pi\chi_{CGS}. \quad (\text{Eq. S50})$$

The magnetic susceptibility for each sample on each magnetometer is given in Table SIX. These fall into the range expected from iron oxide samples.⁶ We see good agreement between the VSM and SQUID values; however, it should be noted that the magnetic susceptibilities measured using the VSM and the SQUID vary within the same order of magnitude (9-11%) despite testing the exact same sample.

Table SIX. SQUID and VSM magnetometry on three batches of iron oxide nanoparticles.

Batch	Sample mass (mg)	$\chi_{SQUID,CGS}$	$\chi_{SQUID,SI}$	$\chi_{VSM,CGS}$	$\chi_{VSM,SI}$	$\chi_{SQUID,SI} - \chi_{VSM,SI}$
1	16.7	0.546	6.86	0.495	6.22	0.64
2	6.6	0.517	6.50	0.459	5.77	0.73
3	6.0	0.499	6.28	n/a ^a	n/a ^a	n/a ^a

a) Batch 3 was not tested on the VSM due to limitations accessing the instrument.

VI.iii. MAP data

The raw and calibrated data as well as the full results from the tests summarized in the main text of the paper are presented in the following sections.

For all MAP tests, the samples were prepared and tested using the same protocols. All iron oxide MNPs were suspended in water via thorough sonication and mixed via vortexing prior to testing in the MAP. Solutions were allowed to come to room temperature prior to MAP testing to avoid temperature-dependent effects on magnetic susceptibility.⁷ Each solution was tested in a disposable poly(methyl methacrylate) (PMMA), standard 3.5 mL spectroscopy cuvette at a volume of 1 mL. The magnetic field was applied immediately when data collection began. Tests were run in the MAP for a duration of 3 minutes, which was determined to be a sufficient length to capture the full system response based on preliminary test steps with this material (iron oxide). Each sample was run in triplicate for reproducibility. Between each test, the sample was aspirated with a pipette at least 10 times to ensure that the MNPs were sufficiently resuspended.

Multi-batch data

All three batches of iron oxide MNPs were tested in the MAP for comparison of the MAP-derived magnetic susceptibility to the SQUID and VSM values. Particles from each batch were suspended in water at a concentration of 100 $\mu\text{g}/\text{mL}$ and tested in the MAP with the 4933 G surface field magnet. Controls of water and batch 1 MNPs tested without a magnet were also run. The raw intensity data is presented in Fig. S15(a)-(c). The data was transformed to concentration over time prior to analysis for magnetic susceptibility and is shown in Fig. S15(d)-(f). The magnetic susceptibility values derived from each MAP trial are given in Table SX.

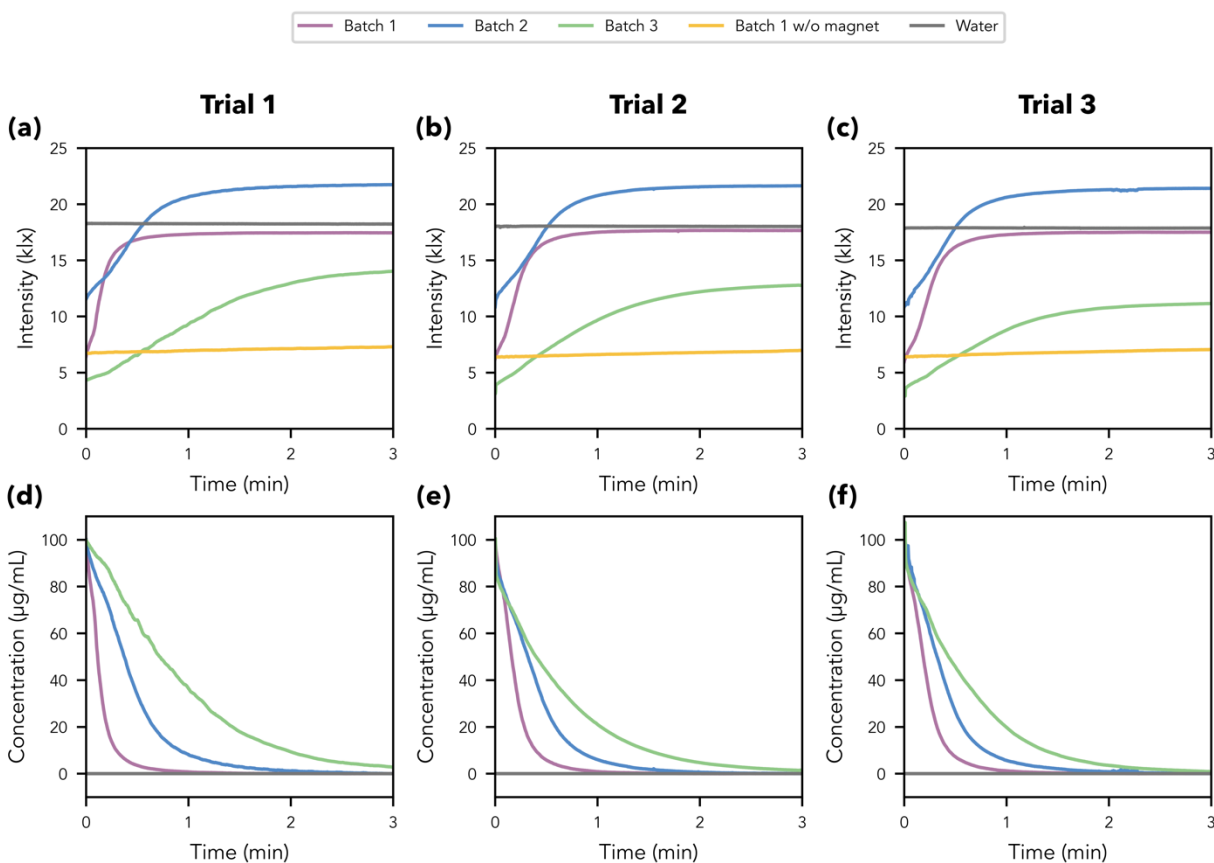


Fig. S15. (a)-(c) Raw MAP data from trials 1, 2, and 3, respectively, using three different batches of iron oxide MNPs suspended in water at a concentration of 100 µg/mL. Two controls were added: water (0 µg/mL) and batch 1 not exposed to a magnetic field. Good reproducibility is observed between trials. **(d)-(f)** The MAP data from trials 1-3, respectively, transformed into concentration over time. Note that the data from the batch 1 with no applied magnetic field were not included because the transformation protocol used in this work requires the signal to fully plateau.

Table SX. Magnetic susceptibilities^a determined by the MAP for iron oxide MNPs from three different batches.

Batch	MAP χ			Avg. $\chi \pm$ Std. Dev.
	Trial 1	Trial 2	Trial 3	
1	5.15	5.64	5.15	5.31 \pm 0.29
2	4.32	4.58	5.76	4.88 \pm 0.77
3	3.40	3.56	3.48	3.48 \pm 0.08

a) All magnetic susceptibilities reported in SI units.

When comparing the raw MAP data between the three batches (Fig. S15(a)-(c)), we can make several observations. First, the batches have different beginning and ending intensity values, which can be explained by the fact that these batches were all tested on different days (and thus the

background intensity measured may vary) and the particle cross-sections vary between batches. More importantly, the intensity increases at different rates: batch 1 has the quickest increase in intensity and batch 3 the slowest increase. This is consistent across all three trials with each batch. This ordering corresponds to the magnetic susceptibilities measured by the MAP when compared across batches. Further, we see the same trend when comparing the SQUID and VSM results to the MAP results (Table SXI).

Table SXI. Magnetic susceptibilities^a derived from MAP measurements relative those derived from SQUID and VSM measurements.

Batch	Avg. MAP χ	SQUID χ	VSM χ
1	5.31	6.86	6.22
2	4.88	6.50	5.77
3	3.48	6.28	n/a ^b

a) All magnetic susceptibilities are reported in SI units. **b)** Batch 3 was not tested on the VSM due to limitations accessing the instrument.

Measurements of varied concentrations

A dilution series was prepared from batch 1 of the iron oxide MNPs to characterize MAP performance across multiple concentrations. Serial dilutions were used to create solutions of iron oxide MNPs at concentrations of 1, 2, 4, 8, 16, 31, 63, 125, 250, and 500 $\mu\text{g}/\text{mL}$ in water. A control of water was also tested. Fig. S16(a)-(c) gives the raw intensity data and Fig. S16(d)-(f) gives the transformed concentration data. The magnetic susceptibility values for the concentrations in the linear working range are given for individual MAP trials in Table SXII.

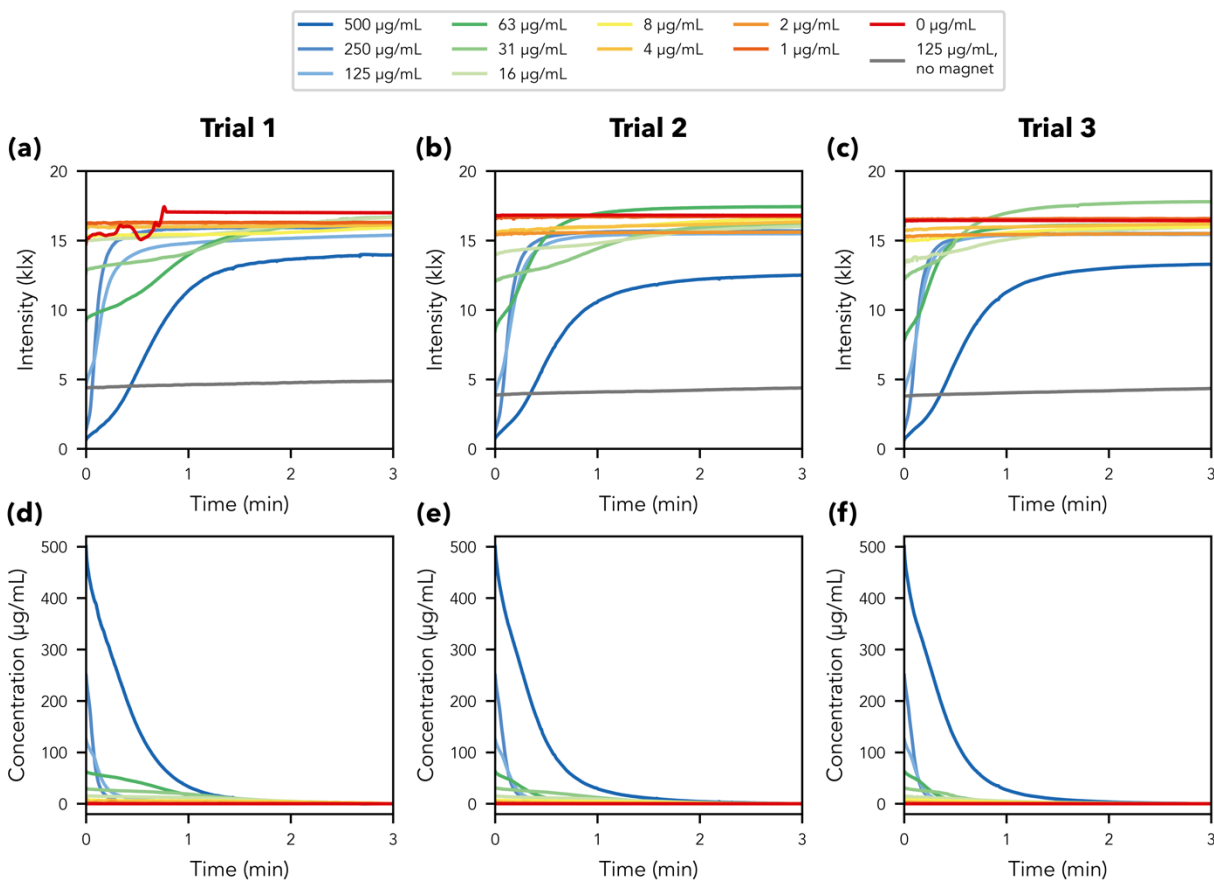


Fig. S16. (a)-(c) Raw MAP data from trials 1, 2, and 3, respectively, using a range of MNP concentrations from 1 $\mu\text{g/mL}$ up to 500 $\mu\text{g/mL}$. Two controls were added: water (0 $\mu\text{g/mL}$) and 125 $\mu\text{g/mL}$ not exposed to a magnetic field. Note that the supernatant of the 500 $\mu\text{g/mL}$ sample appeared translucent but still tinted brown, which could account for the lower final intensity values observed. (d)-(f) The MAP data from trials 1-3, respectively, transformed into concentration over time. Note that the data from the 125 $\mu\text{g/mL}$ with no applied magnetic field were not included because the transformation protocol used in this work requires the signal to fully plateau.

Table SXII. Magnetic susceptibilities^a determined by the MAP for iron oxide MNPs of varied concentrations from the linear range.

Concentration ($\mu\text{g/mL}$)	MAP χ			Avg. $\chi \pm$ Std. Dev.
	Trial 1	Trial 2	Trial 3	
125	5.25	5.16	4.59	5.00 ± 0.36
63	4.14	4.62	5.25	4.67 ± 0.56
31	3.54	4.32	4.12	3.99 ± 0.41
16	3.73	3.84	3.43	3.67 ± 0.21

a) All magnetic susceptibility values reported in SI units.

The raw MAP data shows the same trend shown in Fig. 4 and discussed in section III.ii of the main text. The change in intensity over the duration of the MAP test corresponds to the initial starting concentration of the solution, even over the larger range of initial concentrations (Fig. S16(a)-(c)). However, it should be noted that in the highest concentration tested, 500 $\mu\text{g}/\text{mL}$, the supernatant was translucent brown even after MAP testing, indicating that the solution is likely over saturated. This is reflected in the lower final intensity for all three trials of this concentration. We also note that some trials, such as the first trial with water (Fig. S16(a)) show some noise in the signal, but the overall signal trend is not affected. This emphasizes the importance of using differential measurements, which minimizes the effects of this noise. Once the data is transformed to concentration over time, the trials appear much more consistent within the three trials of a single concentration (Fig. S16(d)-(f)).

The magnetic susceptibilities given in Table SXII appear to show a slightly downward trend as concentration decreases. This is consistent with the theory that suspended nanoparticles will form chains in the presence of an external magnetic field, and as these chains grow, the alignment of dipoles within the chains would increase the magnetic susceptibility.^{8,9} As the concentration decreases, the average distance between MNPs would decrease, result in a lower likelihood of chains forming and a lower average chain length. This could account for the decreased magnetic susceptibility observed as concentration decreases. Still, it is important to note that the MAP-derived magnetic susceptibilities fall into the same order of magnitude as the SQUID-derived values. Because the MAP measures the susceptibility of suspended particles, it may be able to provide information specific to solutions (such as the effect of concentration) that the SQUID cannot, while still providing accurate measurements.

Measurements with varied magnetic fields

In addition, we tested MNP solutions by varying the applied magnetic field. The MNP solution was prepared from batch 1 of iron oxide MNPs at a single concentration of 100 $\mu\text{g}/\text{mL}$. The magnets applied in this work were all neodymium block magnets sourced from K&J Magnetics and had surface fields ranging from 2108 to 4933 G. They are listed with their characteristics detailed in Table SXIII, including the linear approximation used in the model as described in Eq. (S18). Note that all magnets will be referred to by their surface field for simplicity.

Table SXIII. Magnets used in this work and their characteristics.

K&J Magnetics ID	Dimensions (in.)	Grade^a	Surface field (G)^a	Residual Flux Density, B_r (G)^a	Field strength at center of sampling region (G)^b	Linear approximation used in model, $az + b$ (T)^c
BX0X03	1" x 1" x 3/16"	N42	2108	13200	658	-6.677z+0.156
BX0X04	1" x 1" x 1/4"	N42	2704	13200	815	-8.209z + 0.192
BX0X06	1" x 1" x 3/8"	N42	3682	13200	1064	-10.546z + 0.249
BX0X06-N52	1" x 1" x 3/8"	N52	4128	14800	1193	-11.824z + 0.279
BX0X08-N52	1" x 1" x 1/2"	N52	4933	14800	1401	-13.656z + 0.324

a) As reported by K&J Magnetics. **b)** Computed via Eq. (S17) based on the geometry of the MAP. **c)** Described in Eq. (S18). All linear fits had r^2 values > 0.9999. Note that the linear approximation used has units of Teslas; the model was completed in SI units for consistency. Gauss converts to Teslas at a conversion rate of 10000 G to 1 T.

The raw intensity data is presented in Fig. S17(a)-(c), as well as the transformed data (concentration over time) in Fig. S17(d)-(f). The magnetic susceptibility values for each MAP trial at each magnetic field strength except 0 G are given in Table SXIV.

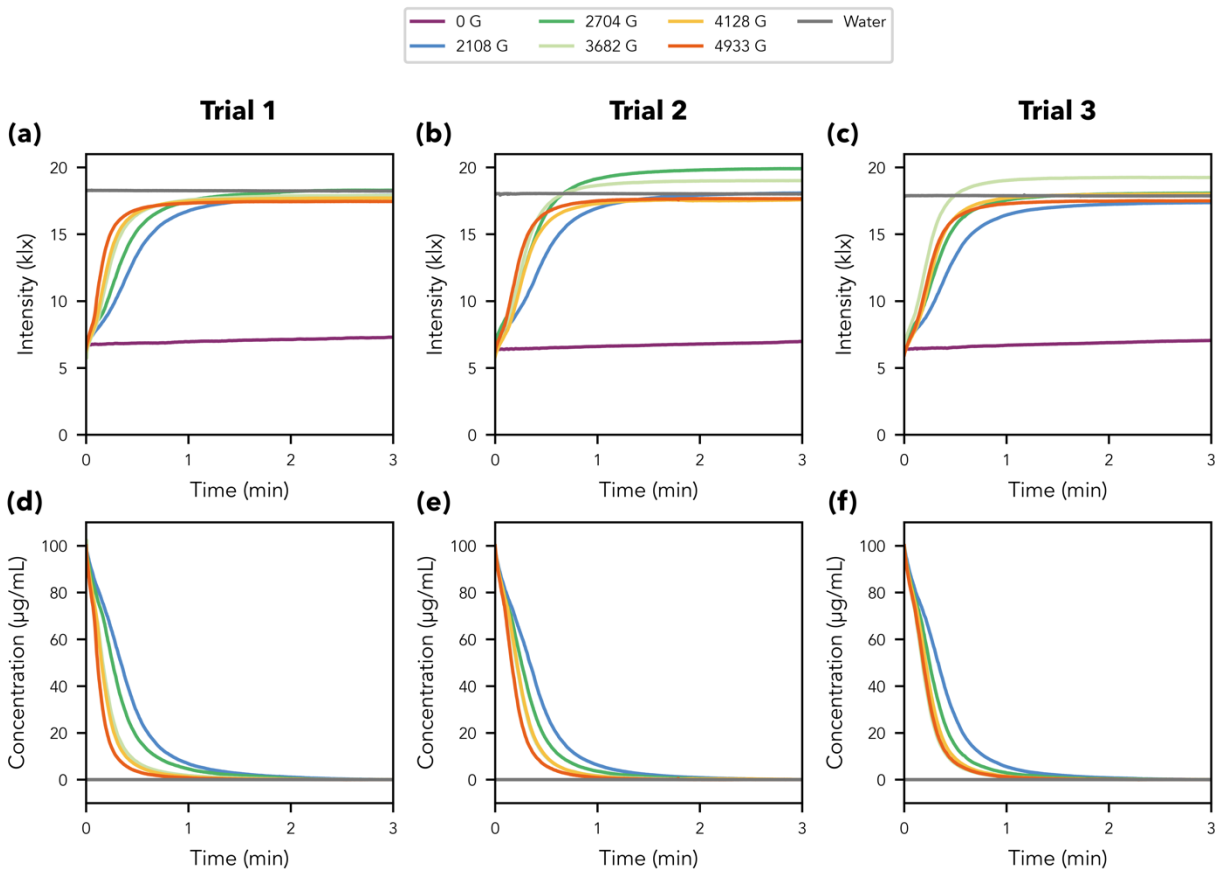


Fig. S17 (a)-(c). Raw MAP data from trials 1, 2, and 3, respectively, of MNPs tested using a range of applied magnets with surface fields from ranging 2108 G to 4933 G. Two controls were added: no magnetic field (0 G) and water exposed to the 4933 G surface field. Each sample was tested at a concentration of 100 $\mu\text{g/mL}$ suspended in water. **(d)-(f)** The MAP data from trials 1-3, respectively, transformed into concentration over time. Note that the data from the 0 G trials were not included because the transformation protocol used in this work requires the signal to fully plateau.

Table SXIV. Magnetic susceptibilities^a determined by the MAP for iron oxide MNPs tested with different applied magnetic fields.

Surface field of applied magnet (G)	MAP χ			Avg. $\chi \pm$ Std. Dev.
	Trial 1	Trial 2	Trial 3	
2108	5.30	6.47	4.67	5.48 ± 0.91
2704	5.20	6.14	5.78	5.71 ± 0.48
3682	4.26	5.02	5.87	5.05 ± 0.81
4128	3.86	5.54	5.12	4.84 ± 0.88
4933	5.15	5.64	5.15	5.31 ± 0.29

a) All magnetic susceptibility values reported in SI units.

Examination of the MAP data reveals several trends. First, we see that the response time increases as the magnetic field strength decreases, a trend discussed in more detail in the next section. This follows intuitively from the definition of magnetic force given by Eq. (S6) and Eq. (S16) indicating that the force would scale with changes to magnetic field.

Second, we also see evidence of the two-phase response discussed in the Data pre-processing section. In many of the trials, there is a clear inflection point when the slope changes abruptly. The time point at which this occurs for each magnetic field strength is shown in Fig. S18. We can see that as the magnetic field strength increases, this time decreases. This supports our hypothesis that the initial phase of the data is from the motion of particles from their resuspension and the inflection point represents the time at which the particle motion is uniformly downward towards the magnet. As the magnetic force increases, the random motion of the particles is overcome quicker, which results in the change of phase of motion occurs earlier in the trial.

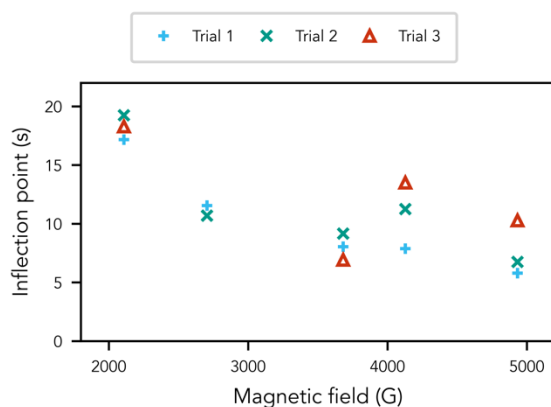


Fig. S18. The magnetic field strength relative to the inflection point. The inflection point was determined to be the time point at which there was a minimum in the time derivative of the concentration data and the concentration began consistently increasing.

Measurements with surface-coated particles

To test the ability of the MAP to complete nondestructive measurements of magnetic susceptibility, we selected a standard commercial MNP and compared the ability of these MNPs that had either been tested in the MAP or not tested to then bind to proteins. We used Dynabeads (ThermoFisher Dynabeads M-280 Streptavidin, #11205D), which consist of an iron oxide core with a polystyrene shell coated with a monolayer of streptavidin.

Biotin-4-fluorescein (fl-biotin, ThermoFisher Biotin-4-Fluorescein, #B10570) binds readily to streptavidin and provides a method to quantify the bioactivity of the Dynabeads through fluorescence. The fl-biotin was initially suspended in dimethyl sulfoxide (DMSO) at a concentration of 5 mg/mL. Aliquots of the fl-biotin were then serially diluted with additional DMSO to produce solutions with concentrations of 3.46 μ M, 0.346 μ M, or 0.0346 μ M.

To show that the streptavidin proteins on the surface were not destroyed, we showed that Dynabeads that had undergone MAP testing could bind the same quantity of biotin as Dynabeads that have not undergone MAP testing (Fig. 6(a) in main text). Aliquots of the original 10 mg/mL

solution of Dynabeads were diluted down to 100 $\mu\text{g}/\text{mL}$ with Dulbecco's phosphate buffer saline (DPBS, ThermoFisher #1404117) at a total volume of 1 mL. The solutions were washed once by separating the Dynabeads with a magnetic rack and removing the supernatant via pipette. DPBS was added to resuspend the solution at a 100 $\mu\text{g}/\text{mL}$ concentration with a volume of 1 mL and the solution was vortexed for 1 minute to resuspend the particles.

The aliquots were grouped into two groups: 1) Dynabead solutions to be tested in the MAP prior to incubation with fl-biotin (2x MAP tested group) and 2) Dynabead solutions to only be incubated with fl-biotin and not undergo prior MAP testing (1x MAP group). Within each of these two groups and in replicates of three, 1 mL solutions of Dynabeads were then incubated with one of three different quantities of biotin (1 pmol, 10 pmol, or 100 pmol) by adding 29 μL of one of the three fl-biotin concentrations (0.0346 μM , 0.346 μM , 3.46 μM , respectively). The solutions were vortexed for 30 seconds after the addition of the fl-biotin and then incubated for 1 hour with gentle rotation at room temperature.

After incubation, all solutions were resuspended by vortexing for 30 seconds and then 1 mL of each were tested in the MAP to separate the magnetic Dynabeads and bound fl-biotin from the supernatant containing the free fl-biotin. The top 10% of the solution (100 μL of the supernatant) was carefully removed from the cuvette, with care not to disturb the separated Dynabeads, and tested in a fluorometer (Molecular Devices SpectraMax M2e) with an excitation wavelength of 494 nm and emission measured at 523 nm. Fluorescence of each solution is given as black circles in Fig. 6(b) in the main text, with the average fluorescence of the three trials represented by the height of the bar. The groups of 2x MAP tested particles and 1x MAP tested particles did not fluoresce with any significant difference from each other but both fluoresced significantly more than the free fl-biotin solution, indicating that MAP testing prior to incubation did not affect the Dynabeads' ability to bind proteins (Fig. 6(b)).

MAP data of the particles tested before biotin binding (from the 2x MAP tested group) is given in Fig. S19 and the magnetic susceptibility values are given in Table SXV.

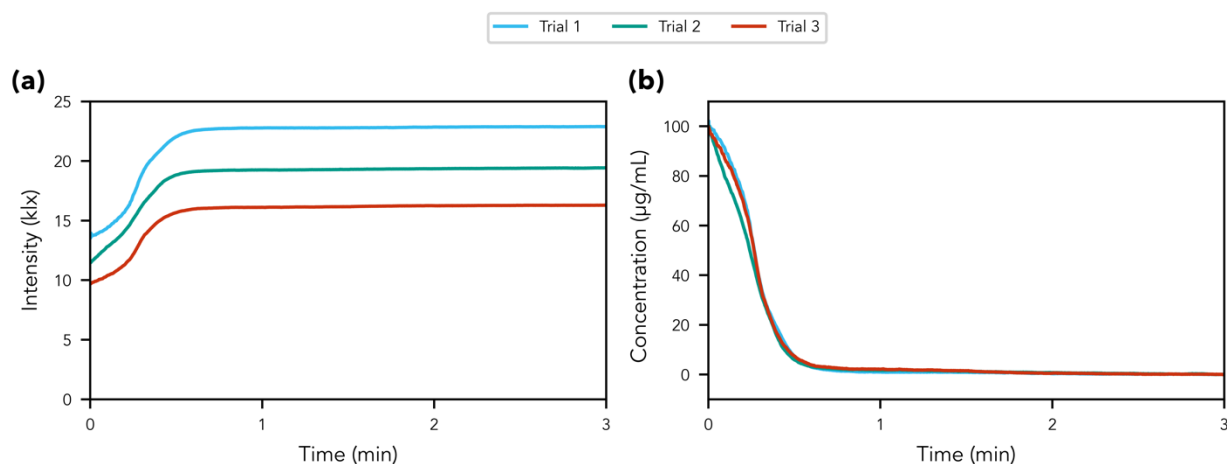


Fig. S19. Dynabeads MAP data shown for 3 trials tested with the 4933 G surface field magnet. **(a)** Raw MAP data. **(b)** Calibrated data.

Table SXV. Magnetic susceptibilities^a of the Dynabeads determined by the MAP.

Trial Number	MAP χ
1	2.56
2	2.74
3	2.61
Avg. $\chi \pm$ Std. Dev.	2.63 \pm 0.09

a) All magnetic susceptibilities are reported in SI units.

VII. Sensor Characterization

Using the datasets from batch 1 of the iron oxide MNPs, we quantified a variety of common sensor characteristics for the MAP.¹⁰ They are summarized in Table SXVI. The metrics and methods are described in more detail in this section.

Table SXVI. Summary of sensor characterization metrics.

Metric	Definition	MAP	Limiting component
Dynamic range	The total range of light intensity that can be detected	~0-30 klux	Optical path (LED and/or light sensor)
Noise level	The level of noise in MAP signal as defined by 3 standard deviations from the mean	16.2 lux (control: water) 21.6 lux (100 μ g/mL MNP sample)	Optical path (LED and/or light sensor)
Working (linear) range	The range of concentrations for which the measured intensity change is a linear function of concentration	16-125 μ g/mL	Optical path (LED and/or light sensor), absorption of MNPs
Saturation Point	The concentration beyond which the measured intensity does not change	~250 μ g/mL	Optical path (LED and/or light sensor), absorption of MNPs
Limit of Detection	The lowest concentration that produces a change in measured intensity signal	2 μ g/mL	Optical path (LED and/or light sensor), absorption of MNPs
Temporal resolution	The average time between measurements	141 ms	Light sensor, microcontroller
Dead time	The time after which the magnetic field is applied before a change in measured intensity is detected	141 ms	Light sensor, microcontroller
Response time	The time after which the magnetic field is applied to the point at which 90% of the change in measured intensity has occurred	22.2-60.8 s (varying magnetic field strengths) ^a	Magnetic field strength, magnetic susceptibility of MNPs

a) See Table SXVII for individual response times for different magnetic field strengths.

VII.i. Dynamic Range

The dynamic range is the total range of light intensity that can be detected by the MAP. This can be limited by a number of factors, including the dynamic range of the light sensor component itself and the intensity of light emitted by the LED, which is affected by the choice of resistors (and thereby the voltage difference across the LED) and manufacturing variation between specific LEDs. Based on our data, the dynamic range of our system was approximately 0-30 klux, but this may vary across the lifetime of the LED.

VII.ii. Noise Level

The noise level quantifies the threshold for noise in MAP signal as 3 standard deviations above the mean measured lux value calculated using a steady state signal (i.e. if a light measurement is 3 standard deviations above the steady state mean, it is considered signal). It is expected to vary with the LED intensity level and the individual light sensor. This value was quantified for two conditions: a control of just water and the 100 $\mu\text{g}/\text{mL}$ MNP sample.

For the control of water, 165 seconds ($n = 1167$ individual data points) from a single trial was used to calculate the noise level. The first 15 seconds were excluded to avoid artifacts related to the application of the magnet (i.e. vibrations causing shifts in cuvette position or waves propagating through the liquid). The distribution of measured intensity values had a standard deviation of 5.4 lux, so we concluded that the noise level for samples of water is 16.2 lux.

For the 100 $\mu\text{g}/\text{mL}$ nanoparticle sample, the last 90 seconds of the trial with the strongest magnet providing a surface field of 4933 G was used to calculate the noise level. This interval of 636 individual data points was selected to provide a large sample size while also being well after the signal had reached a steady state. For the last 90 seconds of a single trial, we found a standard deviation of 7.2 lux, corresponding to a noise level of 21.6 lux. This is comparable to the noise level found for water.

VII.iii. Working (Linear) Range

The working range, or linear range, is the range of sample concentrations for which the output signal, or change in transmission, is directly proportional (linear) to the input concentration. This, along with the saturation point and limit of detection, can be dependent on a number of factors, including the system components (the specific LED and sensor), the wavelength of the light source, the MNP (particularly its cross-sectional size and absorption profile), and the solvent, so this metric could vary significantly. For our system, we found a linear range of about 16 $\mu\text{g}/\text{mL}$ to 125 $\mu\text{g}/\text{mL}$. This also corresponded to the concentration range within which our model performed best (Table SXII). This confers advantages in that the MAP only requires small amounts of sample to take magnetic susceptibility measurements.

This characteristic is shown in the sensor response curve in Fig. 4(b) in the main text.

VII.iv. Saturation Point

The saturation point, also known as the full-scale output, is the sample concentration beyond which the MAP does not measure an increase in the overall change in intensity. We measured this value to be around 250 $\mu\text{g/mL}$ for our system with batch 1 of our MNPs. It should also be noted that at higher concentrations, the MNP solution itself saturates and the MNPs do not fully suspend; this is why concentrations above 500 $\mu\text{g/mL}$ were not tested. The supernatant appears translucent brown instead of clear after MAP testing in samples tested above 250 $\mu\text{g/mL}$ as discussed in Fig. S15(a)-(c).

This characteristic is shown in the sensor response curve in Fig. 4b in the main text.

VII.v. Limit of Detection

The limit of detection (LOD) is the sample concentration below which the MAP does not measure any change in light transmission (i.e. generates no signal). We will define signal as a change in intensity level over the duration of the test that is greater than 3 standard deviations above the change observed for tests with no MNPs (i.e. just the solvent, water). Data from six trials with water are presented previously in the Validation data section of the main text; the first trial from the concentration sweep will be excluded due to the artifact at the initial part of that trial. The mean change in intensity observed in the remaining five trials is 70.3 ± 45.0 lux. Thus, the LOD must have a change in lux greater than 205.3 lux. While we did not optimize around this parameter, opting instead to optimize for cost and accessibility, for our system and nanoparticles, the LOD was approximately 2 $\mu\text{g/mL}$.

This characteristic is shown in the sensor response curve in Fig. 4(b) in the main text.

VII.vi. Temporal Resolution

The temporal resolution, also referred to as the acquisition rate, is defined as the time between measured data points. This value was quantified for six files: 3 tests with water and 3 tests with the 100 $\mu\text{g/mL}$ associated with batch 1 testing. The mean temporal resolution was 141 ms, while the median was 137 ms. The temporal resolution is determined by the integration time of the sensor, which is configured to the minimum value of 100 ms, and the processing time of the microcontroller. The minimum time between measurements actually observed was 131 ms. In contrast, within this subset of 12 data files, the maximum value ranged as high as 273 ms, which we attribute to sporadic increased processing time of the microcontroller. This may correspond to timepoints at which the microcontroller updated the display, which appeared to visually slow the microprocessor at times, but this variation in time between measurements did not appear to ultimately alter performance of the MAP. If necessary, an easy improvement would be to decrease the refresh rate of the display or to use a microcontroller with better processing performance.

VII.vii. Dead Time

The dead time is defined as the time after a stimulus (i.e. the magnetic field) is applied to when a change in signal is observed. In the case of the MAP, this is defined as the time between when the external magnetic field is applied and when the change in light intensity exceeds the noise level.

Note that in our datasets, the magnet is applied manually at approximately $t = 0$ s, but because of human error, the exact timepoint at which the magnet is applied may vary. Even in the 100 $\mu\text{g}/\text{mL}$ samples with the lowest applied magnetic field, a surface field of 2108 G, the light transmission increases at a rate faster than the acquisition rate of our system, which is 141 ms on average. Therefore, at this sample concentration and applied magnetic field strength the dead time is equal to (and limited by) the acquisition rate of 141 ms. We would expect the dead time to potentially increase with decreasing sample concentration or decreasing magnetic field strength.

VII.viii. Response Time

The response time is defined as the time period after which the stimulus (i.e. the magnetic field) has been applied to the point at which 90% of the change in measured light intensity has occurred. This value was quantified for each of the non-zero multi-magnet series trials testing a 100 $\mu\text{g}/\text{mL}$ solution. The results are presented in Fig. 5(b) in the main text, and in more detail in Table SXVII. Generally, the response time decreased with increasing applied magnetic field strength, which is as expected since the MNPs would experience a greater magnetic force. Importantly, because these response times are so short, they facilitate a short test duration. The duration of 3 minutes used in this work gives a wide margin from the response times to ensure capture of the full MNP response while still being significantly shorter than other magnetometer data collection protocols, but trial lengths of 2 minute or even 1 minute may still be sufficient to capture the full response in some cases.

Table SXVII. Response times for different applied magnets.

Surface field of applied magnet (G)	Response time (s)			Avg. response time \pm std. dev (s)
	Trial 1	Trial 2	Trial 3	
2108	60.8	59.1	56.2	58.7 \pm 2.4
2704	51.0	47.3	42.6	47.0 \pm 4.2
3682	32.6	35.9	30.8	33.1 \pm 2.6
4128	29.1	35.8	35.0	33.3 \pm 3.7
4933	22.2	28.8	31.8	27.6 \pm 4.9

VIII. Troubleshooting

During our validation testing, we noticed and solved several possible issues. A short description of possible solutions to these problems are provided here.

VIII.i. LED Stabilization

The optical source (LED) must stabilize before beginning to use the system; otherwise, artifacts will be present in the measurement as the initial incident intensity may rise independent of the signal from the MNPs. For the specified LED, SparkFun COM-00528, the stabilization time was

about 30 minutes (Fig. S20), but we recommend running an initial screen of an hour after the MAP is first assembled to determine how long the LED needs to warm up as this may vary for each LED. The warmup screen shown when the MAP is first powered can also be used to manually monitor the LED brightness as it warms up.

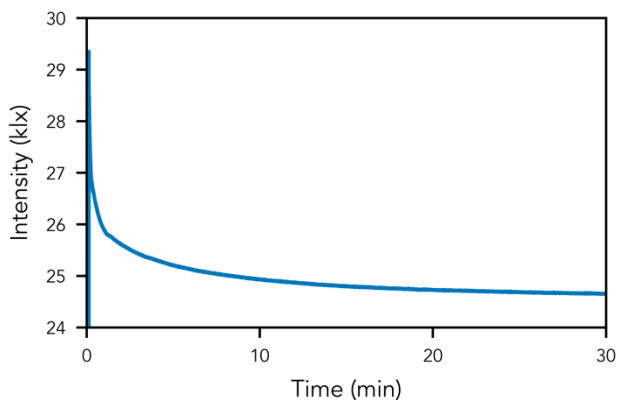


Fig. S20. Measured LED intensity over time. The signal plateaus after about 30 minutes, in agreement with the LED datasheet. Note that the initial jump is the LED being turned on.

VIII.ii. Low Optical Signal

If the light intensity signal is very low (less than 10k lux) without a solution of nanoparticles, there are a few possible causes.

If the MAP has just been assembled, it is possible that the light sensor is not oriented properly. It should be oriented so that the text on the board is right side up, as described in Step 5a of Hardware Assembly (Fig. S10(b)).

If the LED light seems dim, it is possible that the current through the LED is not sufficiently high. Measure either the voltage through the LED with a multimeter and calculate the LED current or directly measure the current through the LED and compare it to the manufacturer's listed forward current for the LED. If it is lower, choose appropriate resistor values based on Eq. (S49) and replace the resistors in the LED circuit (Fig. S5). If the LED brightness is lower despite the ideal current flowing through the LED, then the LED may need to be replaced.

VIII.iii. Nanoparticle Settling and Clumping

The measurement is dependent on the interaction of the MNPs with the optical field. Therefore, it is important that the nanoparticles are uniformly distributed throughout the optical field. As has been discussed in prior works, there are several mechanisms that can lead to non-uniform distributions, resulting in measurement artifacts.¹¹

Among the potential mechanisms, the most commonly observed effects during the present work were MNP settling and clumping in the solutions. While particle clumping was able to be avoided by using optimized sample concentrations, MNP settling required active monitoring and mitigation controls. Specifically, whenever a solution is tested in the MAP, it was thoroughly shaken, vortexed, or sonicated to completely re-disperse the MNPs in solution prior to taking a

measurement. This is particularly true when running a repeated test, as MNP clumping may occur when the MNPs are aggregated at the bottom of the solution.

IX. References

- ¹ A.Md.R. Kabir, D. Inoue, Y. Kishimoto, J. Hotta, K. Sasaki, N. Kitamura, J.P. Gong, H. Mayama, and A. Kakugo, “Drag force on micron-sized objects with different surface morphologies in a flow with a small Reynolds number,” *Polym J* **47**(8), 564–570 (2015).
- ² M.A.M. Gijs, “Magnetic bead handling on-chip: new opportunities for analytical applications,” *Microfluid Nanofluid* **1**, 22–40 (2004).
- ³ S.S. Shevkoplyas, A.C. Siegel, R.M. Westervelt, M.G. Prentiss, and G.M. Whitesides, “The force acting on a superparamagnetic bead due to an applied magnetic field,” *Lab Chip* **7**(10), 1294–1302 (2007).
- ⁴ T.G. Mayerhöfer, S. Pahlow, and J. Popp, “The Bouguer-Beer-Lambert Law: Shining Light on the Obscure,” *ChemPhysChem* **21**(18), 2029–2046 (2020).
- ⁵ A. Scholtz, J. Paulson, and V. Nuñez, “Magnetophotometer (MAP) GitHub Repository,” (n.d.).
- ⁶ B.A. Maher, “Magnetic properties of modern soils and Quaternary loessic paleosols: paleoclimatic implications,” *Palaeogeography, Palaeoclimatology, Palaeoecology* **137**(1–2), 25–54 (1998).
- ⁷ S. Mugiraneza, and A.M. Hallas, “Tutorial: a beginner’s guide to interpreting magnetic susceptibility data with the Curie-Weiss law,” *Commun Phys* **5**(1), 1–12 (2022).
- ⁸ V. Reichel, A. Kovács, M. Kumari, É. Bereczk-Tompa, E. Schneck, P. Diehle, M. Pósfai, A.M. Hirt, M. Duchamp, R.E. Dunin-Borkowski, and D. Faivre, “Single crystalline superstructured stable single domain magnetite nanoparticles,” *Sci Rep* **7**(1), 45484 (2017).
- ⁹ E. Myrovali, N. Maniotis, A. Makridis, A. Terzopoulou, V. Ntomprougkidis, K. Simeonidis, D. Sakellari, O. Kalogirou, T. Samaras, R. Salikhov, M. Spasova, M. Farle, U. Wiedwald, and M. Angelakeris, “Arrangement at the nanoscale: Effect on magnetic particle hyperthermia,” *Sci Rep* **6**(1), 37934 (2016).
- ¹⁰ H.K. Hunt, and A.M. Armani, “Label-free biological and chemical sensors,” *Nanoscale* **2**(9), 1544 (2010).
- ¹¹ Z. Boekelheide, and C.L. Dennis, “Artifacts in magnetic measurements of fluid samples,” *AIP Advances* **6**(8), 085201 (2016).